The electrical properties of Titan's surface at the Huygens landing site measured with the PWA-HASI Mutual Impedance Probe. New approach and new findings

Michel Hamelin, Anthony Lethuillier, Alice Le Gall, Réjean Grard, Christian Béghin, Konrad Schwingenschuh, Irmgard Jernej, José-Juan López-Moreno, Vic Brown, Ralph D. Lorenz, et al.

The electrical properties of Titan's surface at the Huygens landing site measured with the PWA-HASI Mutual Impedance Probe. New approach and new findings

Michel Hamelin[1,2*], Anthony Lethuillier [1,2], Alice Le Gall[1,2], Réjean Grard[3], Christian Béghin[4], Konrad Schwingenschuh[5], Irmgard Jernej[5], José-Juan López-Moreno[6], Vic Brown[6], Ralph D. Lorenz[7], Francesca Ferri[8], Valérie Ciarletti[1,2]

[1] Sorbonne Universités, UPMC Univ. Paris 06, LATMOS-IPSL, UMR 8190, 75005 Paris, France.

[2] Univ. Versailles St-Quentin; CNRS/INSU, LATMOS-IPSL, UMR 8190, 78280 Guyancourt, France.

[3] Prinses Margrietlaan 7, 2341VJ Oegstgeest, The Netherlands and 11 rue des Forges, Paunay, 79400 Saivres France; retired from the European Space Agency, ESTEC, Noordwijk, The Netherlands.

[4] LPC2E, CNRS, 3A Avenue de la Recherche Scientifique, 45071 Orléans Cedex, France.

[5] Space Research Institute, Austrian Acad. of Sciences (IWF), Schmiedlstrasse 6, 8042 Graz, Austria.

[6] Instituto de Astrofísica de Andalucía (IAA), CSIC, P.O. Box 3004,18080 Granada, Spain.

[7] JHU/APL, Laurel,MD, United States

[8] Università degli Studi di Padova, Centro di Ateneo di Studi e Attività Spaziali "Giuseppe Colombo", via Venezia 15 35131 Padova, Italy.

Abstract

Ten years after the successful landing of the Huygens Probe on the surface of Titan, we reassess the derivation of ground complex permittivity using the PWA-MIP/HASI measurements (Permittivity, Waves and Altimetry-Mutual Impedance Probe/Huygens Atmospheric Structure Instrument) at the frequencies 45, 90 and 360 Hz. For this purpose, we have developed a numerical method, namely "the capacity-influence matrix method", able to account for new insights on the Huygens probe attitude at its final resting position. We find that the surface of Titan at the landing site has a dielectric constant of 2.5±0.3 and a conductivity of 1.2±0.6 nS/m, in agreement with previously published results but with much more reliable error estimates. These values speak in favour of a photochemical origin of the material in the first meter of the subsurface. We also propose, for the first time, a plausible explanation for the sudden change observed by PWA-MIP ~11 min after landing: this change corresponds to a drop in the ground conductivity, probably due to the removal of a superficial conductive layer in association with the release of volatile materials warmed by the Huygens Probe.

Keywords: Titan; Titan surface; Satellite surfaces; Data reduction techniques

*Corresponding author :   Michel Hamelin
                                    LATMOS-IPSL / UPMC
                                    Tour 45, C 45-46, E3 (boite 102)
                                    4 place Jussieu 75252 Paris CEDEX 05
                                    France
                                    Tel. : +33144272163
                                    Email : michel.hamelin@latmos.ipsl.fr

1. Introduction

Ten years after the descent of the Huygens probe in the atmosphere of Titan and its successful landing on the surface (Lebreton et al., 2005), the scientific context has significantly evolved. More than one hundred flybys of the Cassini Saturn-orbiter have brought an extensive view on the diversity of the landscape and of the surface features: lakes in high latitude regions, dune fields in the equatorial belt, mountains, channel networks (e.g. Jaumann et al., 2008; Lopes et al., 2010; Radebaugh et al., 2011; Le Gall et al., 2012), and although the in-situ measurements performed at the Huygens landing site cannot be regarded as representative of the entire surface, they provided an invaluable ground truth for Cassini remote measurements.

The Huygens probe (Lebreton and Matson, 2002, and Fig. 1a) landed on Titan, on 14 January 2005, at a latitude of 10.3° S and a longitude of 167.6° E (Karkoschka et al., 2007), fortunately 'on a relatively soft solid surface whose properties are analogous to wet clay, lightly packed snow and wet or dry sand' (Zarnecki et al., 2005). The temperature and pressure measured at the surface by the Huygens Atmospheric Structure Instrument (HASI) were 93.65 ± 0.25 K and 1471 ± 1 hPa (Fulchignoni et al., 2005). The landing site appears to be relatively flat and strewn with 2-20-cm sized, likely water ice mixed with organics cobbles lying on a dry river bed (Tomasko et al., 2005). Observations from the Cassini Visual and Infrared Mapping Spectrometer (VIMS) on 26 October 2004 prior to the release of the probe suggested that the landing site area was not liquid (Sotin et al., 2005) contrary to what was anticipated. However, the presence of at least some liquid hydrocarbons in the close subsurface was indicated unambiguously by the detection of CH_4 and C_2H_6 by the Gas Chromatograph Mass Spectrometer (GCMS) during its operation on the ground, where its heated inlet caused the release of hydrocarbons (Niemann et al., 2005, 2010; Williams, McKay and Persson, 2012). Additional evidence of dampness was provided by the temperature evolution of the inlet (Lorenz et al., 2006), the possible formation of a dewdrop on the camera baffle (Karkoschka and Tomasko, 2009), and the suppression of ultrasound propagation in a Surface Science Package (SSP) instrument, probably by the evolution of absorbing vapours (Lorenz et al., 2014). SSP was mostly dedicated to the physical characteristics of the surface, either solid or liquid (Zarnecki et al., 2002; Zarnecki et al., 2005; Leese et al., 2012): close remote sensing of the surface was performed by the active

SSP Acoustic Properties sensor (API-S) that detected specular properties compatible with a wet and smooth surface (Towner et al., 2006) as well as by the HASI Radar Altimeter Extension (RAE) which is part of the Permittivity, Waves and Altimetry (PWA) instrument (Fulchignoni et al., 2002, 2005). The characterization of Titan's surface physical and chemical properties at the landing site is completed with the in situ measurements of the complex permittivity (dielectric constant and electric conductivity) with the Mutual Impedance Probe (PWA-MIP), which is the subject of this paper.

The PWA analyser (Grard et al., 1995), a unit of the HASI instrument (Fulchignoni et al., 2002) was designed for investigating the electric properties and other related physical characteristics of the atmosphere of Titan, from an altitude of around 140 km down to the surface (Fig.1). PWA consists of a Mutual Impedance Probe (MIP) that measures the voltage difference between two electrodes RX1 and RX2 that is induced by the current flowing between two other electrodes TX1 and TX2. The volume -and depth- of the near-surface explored by PWA-MIP in its surface mode of operation is commensurate with the distances between electrodes, namely 0.5-1.0 m. PWA also includes two Relaxation Probes (RP), RP1 and RP2 that are initially biased at a DC potential with respect to the lander structure and then allowed to return to their equilibrium potential due to the collection of charged particles from the environment. During the descent, both MIP and RP measurements led to the discovery of electron and ion density layers in the lower atmosphere. (Fulchignoni et al., 2005; Grard et al., 2006; Simões, 2007, Hamelin et al., 2007; López-Moreno et al., 2008), and revealed the existence of an atypical Schumann resonance that implies the presence of a subsurface water ocean (Béghin, Hamelin and Sotin, 2010). Following the successful landing of Huygens, the operation of PWA was extended for approximately 32 min measuring the electrical properties of the ground until the end of the HASI measurement cycle, and also recording the weak 36 Hz signal of the Schumann resonance (Béghin et al., 2013), while the data link to the orbiter lasted for 40 min more (Pérez-Ayúcar et al., 2006).

A first very preliminary estimate of the ground dielectric constant (~2) was published in Fulchignoni et al. (2005). Grard et al. (2006) later constrained the dielectric constant in the range 2-3 and provided a rough estimate of the conductivity of ~0.4 nS/m. In this paper, we refine the analysis of the PWA-MIP data, accounting, in particular, for new insights on the final resting position of the Huygens capsule. Grard et al. (2006) also noted a sudden change

in the PWA-MIP measurements, recorded about 11 min after the Huygens landing. This change is probably related to a change of electrical properties of the first layer of the surface but no developed explanation was advanced to explain it before the present work.

In section 2, we give a technical description of the PWA-MIP/HASI instrument. We present an overview of the PWA-MIP data set, in section 3, prior to its analysis. Section 4 deals with the analytical derivation of the ground complex permittivity assuming an idealized quadrupole configuration, homogeneous environments, and plane interfaces, whereas section 5 describes a numerical modelling technique that we have developed, a technique much more appropriate to realistic cases. This technique is then used for the analysis of the PWA-MIP data collected on the surface of Titan as described in section 6. Reliable estimates of both the dielectric constant and the electrical conductivity are inferred. The sudden change of the apparent permittivity ~11 min after the landing is investigated. This latter observation raises the question of the possible existence of a temporary superficial layer, a hypothesis that is considered in section 7 with some tentative explanations for this phenomenon. Section 8 is dedicated to summary and conclusions.

2. The PWA-MIP/HASI instrument on the Huygens Probe

2.1 The science payload of the Huygens Probe and the HASI package

The Huygens probe carries a set of complementary instruments. It may be useful to recapitulate the composition of the payload as the analysis of the PWA-MIP data also involves information collected by other instruments. A detailed description of the probe and of the mission can be found in Lebreton and Matson (2002), which shows the location of the main instrument sensors (Fig. 1a): i) the HASI sensors on two deployable booms system (DBS) and on the stub, ii) the Gas Chromatograph and Mass Spectrometer (GCMS), iii) the Aerosol Collector and Pyroliser (ACP), iv) the Surface Science Package (SSP), v) the Descent Imager / Spectral Radiometer (DISR), vi) the accelerometer located close to the probe center of mass that is not visible.
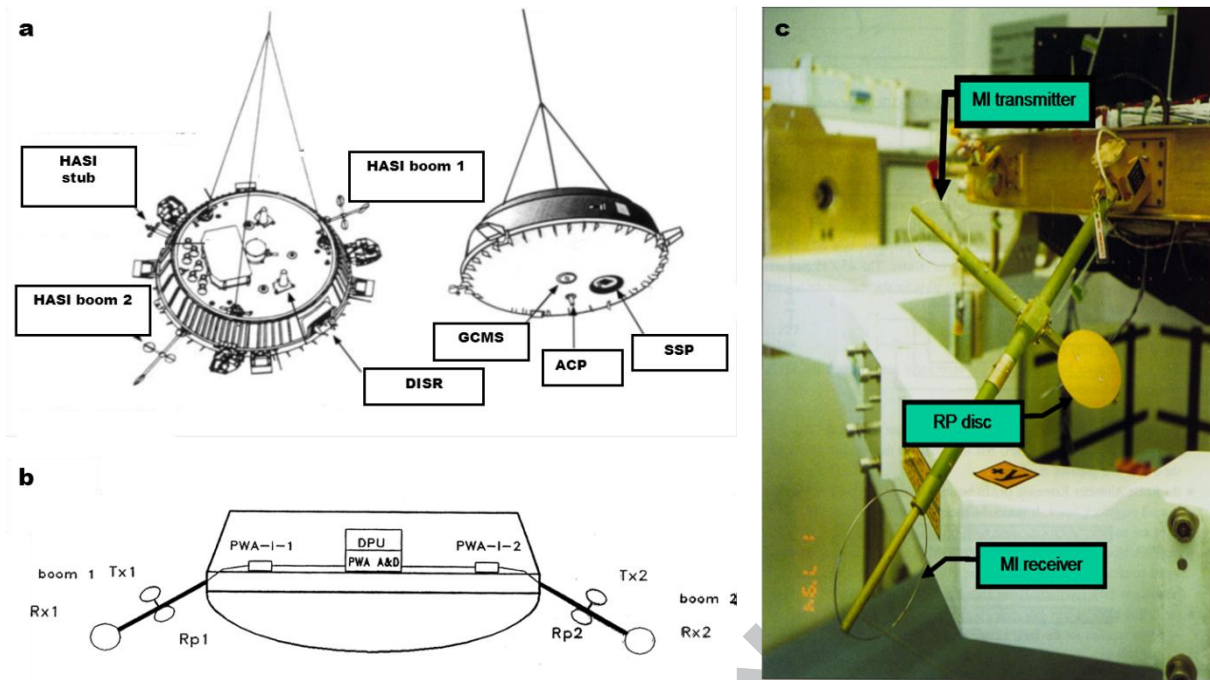
Figure 1. Sensors on the Huygens Probe. a) Locations of the main payload sensors and PWA booms (adapted from Lebreton and Matson (2002)). b) The PWA sensors and electronic boxes; TX1 and TX2, Transmitter electrodes; RX1 and RX2, Receiver electrodes RP1 and RP2, Relaxation Probes. c) A view of one boom showing the MIP and RP electrodes.

HASI (Fig. 2a) consists of a central processor unit (CPU) that relays both commands and data between the PWA digital signal processor (DSP) and the Huygens telemetry systems. The DSP, on the PWA-D board processes the PWA measurements and delivers telemetry packets to the HASI CPU. A detailed description can be found in Falkner (2004).

2.2 The PWA-HASI instrument

Most of PWA sensors, and in particular the MIP and RP electrodes, are installed on the deployable booms. The signals are processed by the analog board PWA-A. A microphone (ACU) attached to the stub and a radar altimeter extension (RAE) that is sensitive to ground permittivity and roughness are not considered in this study. The RAE signals from the two Huygens radar altimeters are processed in PWA-D and the analysis of the data collected before landing has been recently reported in Lorenz et al. (2015).
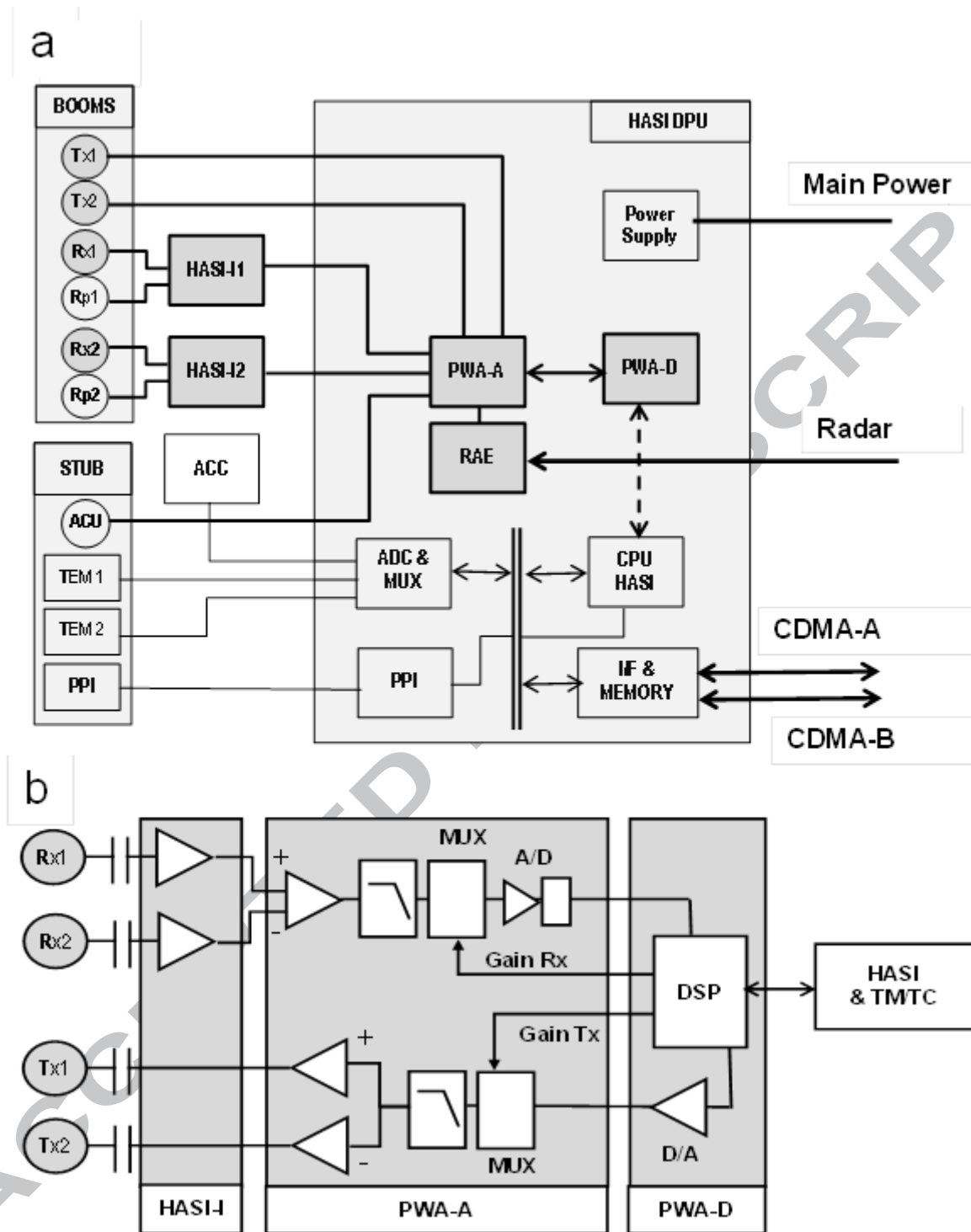
Figure 2. a) HASI block diagram with PWA elements indicated in dark grey. The PWA sensors are mounted on two deployable booms and the HASI temperature sensors on a fixed stub. b) Detailed PWA block diagram showing the PWA-I1 and PWA-I2 preamplifiers and the PWA-A board. Commands and data are handled by the HASI Digital Processing Unit (DPU).

The two booms together carry six electrodes (Figs. 1b, 1c and 2a): two transmitter and two receiver rings for the Mutual Impedance Probe (MIP), and two Relaxation Probe (RP) disks. In order to minimize stray capacitance, no electrical connectors are included in the wiring between the sensors and the HASI-I boxes, where the signals are fed to the PWA-A board through buffer amplifiers with low output impedance.

2.3 The main characteristics of PWA-MIP

The PWA-MIP instrument is operated in two modes. The passive mode is dedicated to the study of natural electrostatic waves. The active modes consist of mutual impedance measurements designed to determine the complex permittivity of the surrounding medium, in the atmosphere or on the surface of Titan.

The PWA-MIP electrode configuration is shown in Figs. 1b and 1c and the electronic circuit is schematically represented in Fig. 2b. A more detailed description can be found in Hamelin et al. (2007) and Falkner (2004).

Transmitting circuit. The TX electrodes consist of rings with a diameter of 65 mm and their capacitance is 1.85 pF in vacuum. A sinusoidal voltage of known amplitude is applied to the TX1 and TX2 electrodes through small coupling capacitances of 0.43 pF ±20% (Trautner and Falkner, 2000), so that the injected current be less dependent of the electrode impedances in the medium. The current emitted by the transmitting electrodes is unfortunately not measured. The influence of the medium is small but the emitted current is not strictly independent of the environment.

Receiving circuit. The RX electrodes consist of rings, 100 mm in diameter with capacitances of 2.64 pF in vacuum. They are connected to the preamplifiers through ~0.4 pF capacitors. The preamplifiers (HASI-I modules) are accommodated within the Huygens capsule, at 'room' temperature, whereas the RX (and TX) coupling capacitors are mounted outside, next to the electrodes, at Titan temperature. The connections are made with triaxial cables; the inner shield is an active guard driven by the preamplifier. More details on the receiving circuit are reported in Annex II.

Relaxation Probe (RP). An RP electrode, a disc 70 mm in diameter, is mounted next to each TX electrode. RP1 is connected to a very high impedance electrometer and its DC potential is floating, while RP2 is connected to the Huygens structure (which serves as a

reference potential) through a 352 pF capacitor that must be taken into account in the electric circuit model.

Analog circuitry. The circuits also play the role of filters and adjust the signal levels for conversion to digital values (Fig.2b).

MIP working frequencies. MIP operates at a frequency of 45 Hz in the atmospheric mode. There are four additional frequencies in the ground mode, namely 90 Hz, 360 Hz, 1440 Hz and 5760 Hz.

3. Overview of the PWA-MIP raw data

The PWA-MIP data consist in successive measurements of the voltage difference ΔV between the two receiving electrodes. The signals from each electrode are fed into a differential amplifier before being processed by an Analog to Digital Converter (ADC). The numerical waveforms are analysed by a digital signal processor (DSP) which provides, through the telemetry, the complex voltage (real and imaginary parts) at ADC level, V_{ADC}. The amplitude and phase versus time of the signal V_{ADC} are shown in Fig. 3 for the five working frequencies. The emitted current is not measured.

3.1 The last atmospheric measurements as the vacuum reference

The permittivity of a neutral atmosphere is close to that of vacuum and the last 8 PWA-MIP measurements at 45 Hz before landing are used as a reference for evaluating the atmospheric conductivity at higher altitudes (Hamelin et al., 2007). These reference measurements are represented by green dots in Fig. 3a. The mean amplitude of V_{ADC} is 1.842 V. This value is corroborated by the MIP measurements collected during the descent at altitudes of 99.7 ± 1.3 km (around 1057 s mission time), when the RP relaxation exhibits a plateau (López-Moreno et al., 2008), associated with the absence of free electrons probably due to their attachment onto aerosols. The two values of the amplitudes of V_{ADC} measured were then 1.826 V and 1.884 V. There are, unfortunately no "vacuum" references at higher frequencies, because the only operating frequency during descent was 45 Hz.
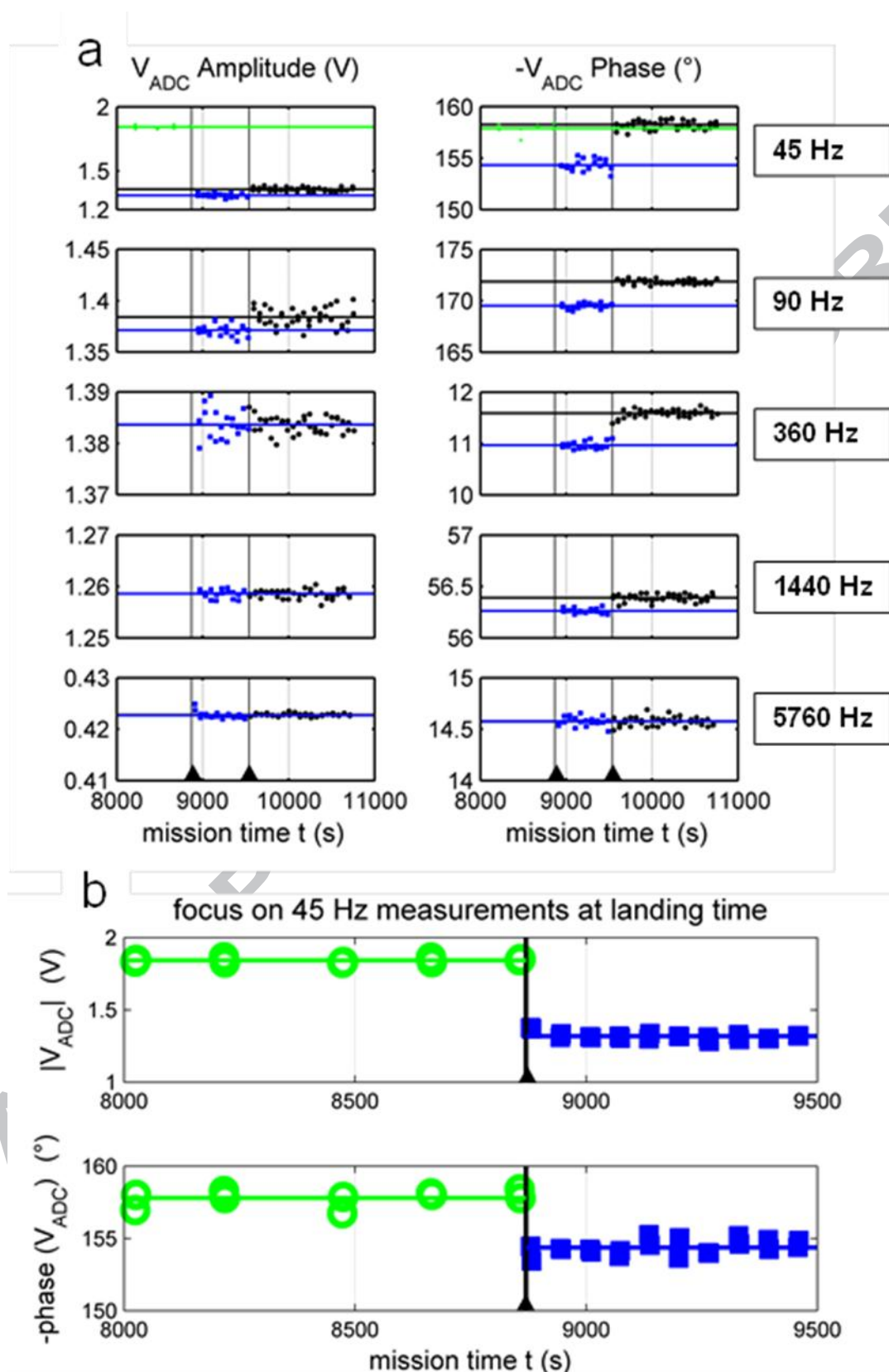
Figure 3. PWA-MIP receiver signal at the ADC output vs. mission time: a) Amplitude (left) end phase (right), for the 5 operation frequencies 45, 90, 360, 1440, and 5760 Hz (from top to

bottom). The green dots in the upper panels are the last measurements at 45 Hz before touch down (marked with a vertical line at t = 8870); the average amplitude and phase (green lines) serve as references; the discontinuity at 9539 s mission time (also marked) is shown in more detail in Fig. 9. Horizontal lines show the mean values of amplitude of phase, before (blue) and after (black) that time. b) Zoom on the landing event. The MIP instrument performs two consecutive measurements at 2 s time intervals and the time interval between twin measurements is 192 s for the atmospheric mode and 64 s for the surface mode.

3.2 The surface measurements

All surface measurements at the ADC input are shown in Fig. 3a for the five working frequencies. They show a discontinuity in both amplitude and phase ~11 min after landing (i.e., mission time 9535 s). The step is more significant at lower frequencies and more visible on the phase. However it seems to be absent at 5760 Hz.

At a first glance, this intriguing feature is either an artefact or reflects an evolution of the medium around the probe. At 360 Hz, two phase measurements taken at 2 s interval give a scale of the order of 4 s for the extremely short duration of the transition. The PWA-MIP surface data analysis will enable us to compare the properties of the environment before and after the event as discussed in sections 6-7 and with the support of Fig. 10.

4. Derivation of the complex permittivity from mutual impedance measurements. Analytical theory.

4.1 A brief historical account

The design of the PWA-HASI Mutual Impedance Probe on Huygens is derived from the DC quadrupolar probe first developed by Wenner (1915) to evaluate the terrestrial ground conductivity through the measurement of the conductance which is the ratio of the DC voltage on a receiving dipole to the DC current injected into the medium by a transmitting dipole. In a perfectly homogeneous medium, the same goal can be achieved more simply with a self-impedance probe (i.e., with only one TX electrode and one RX electrode). However the MIP

technique is less sensitive to poor contacts between the electrodes and the medium and to local inhomogeneities around the electrodes. This technique was successfully used in space by Storey et al., 1969, with AC signals during several ionospheric and magnetospheric missions around the Earth (Hamelin et al. 2007 and references therein). The idea to transpose the original DC Wenner quadrupolar technique to study planetary surfaces was first introduced by Grard (1990a; 1990b), who proposed an AC arrangement for the Huygens probe. Although the main goal of Huygens was the study of the atmospheric conductivity of Titan, a surface mode was proposed for PWA-MIP in order to infer the complex permittivity of the ground, i.e., the dielectric constant and the conductivity.

4.2 Quadrupole with point electrodes within a homogeneous medium

In the frequency range of PWA-MIP we can assume a quasi-static regime and ignore the magnetic induction. We also neglect the influence of the wires and consider an oscillating point charge $q = q_0 \exp(i\omega t)\delta(\mathbf{r})$, where ω is the pulsation, t the time, $i = \sqrt{-1}$, and $\delta(\mathbf{r})$ the 3D Dirac function. The medium is infinite and homogeneous with a dielectric constant ε_r and a conductivity σ.

With harmonic functions of the form $\exp(i\omega t)$, the Ampère-Maxwell equation:

$$\mathbf{j} + \sigma \mathbf{E} + i\omega \varepsilon_0 \varepsilon_r \mathbf{E} = \mathbf{0}$$

where $\mathbf{j}$ and $\mathbf{E}$ are the current density and the electric field vectors, is written:

$$\mathbf{j} + i\omega\varepsilon_0 \varepsilon^* \mathbf{E} = \mathbf{0} \text{, with } \varepsilon^* = \varepsilon_r - i\, \varepsilon_i \text{ , and } \varepsilon_i = \sigma/\varepsilon_0\,\omega. \tag{1}$$

ε^* is the normalized complex permittivity. The complex potential V_δ around the point charge $q\,\delta(\mathbf{r})$ is derived from its value in a vacuum by replacing the permittivity constant ε_0 by the complex permittivity $\varepsilon_0\,\varepsilon^*$:

$$V_\delta(\mathbf{r}) = \frac{q}{4\pi r \varepsilon_0\,\varepsilon^*} = -\frac{i\,I_\delta}{4\pi r\omega\varepsilon_0\varepsilon^*} \quad \text{for } r \neq 0 \tag{2}$$

where $I_\delta = dq/dt$ is the current injected into the medium and r is the radial distance.

The potential generated by a dipole formed by two opposite point charges is easily derived from Eq. (2), as well as the potential difference ΔV between two point electrodes forming a receiving dipole. The mutual impedance of the quadrupole is then defined as $Z = \Delta V/I_\delta$ (Grard, 1990b). It results that the normalized mutual impedance of a quadrupole, that is the ratio of its value in the medium Z to that in a vacuum Z_0, is:

$$Z_N = Z/Z_0 = 1/\varepsilon^*. \tag{3}$$

4.3 Quadrupole with point electrodes in presence of a plane interface between two homogeneous media. Electrostatic images theory.

The case of a quadrupole either above or embedded into a ground of permittivity ε* is solved analytically in Grard (1990a; 1990b) using the electrostatic image theory. When the point electrodes are lying on the ground and the atmosphere has the permittivity of the void, the normalized mutual impedance can be simply expressed as:

$$Z_N = \frac{2}{(1+\varepsilon^*)} \tag{4}$$

that is the mutual impedance of an infinite medium with the average permittivity of the two media.

These analytical results are useful but can only be used as guideline, especially in the case of the PWA-MIP experiment in which the environment of the electrodes has a non-negligible effect on the measurements. In particular, the proximity of the conductive Huygens capsule (the electrodes are accommodated on ~50 cm booms, see Fig. 1) was found to modify the mutual impedance by ~18% (Cadène, 1995). While this difficulty can be partially addressed by modelling the capsule as a sphere, using again the electrostatic image theory (Hamelin et al., 2000), numerical modelling of the instrument environment is required to reach the desired accuracy of the estimation of the electrical properties of the ground.

5. Derivation of the surface complex permittivity from PWA-MIP measurements: numerical technique.

In this section we describe the approach developed to analyze the PWA-MIP data. This approach is called "the matrix influence-capacity method".

5.1 First approach

The PWA-MIP data consist exclusively of potential difference measurements between RX1 and RX2. As mentioned before, the injected current is not measured but the transmitter electrodes TX1 and TX2 are connected to the generator through coupling capacitors. If the

corresponding capacitances were small enough, the injected current could be assumed constant and Z_N would simply be equal to the normalized voltage difference $\Delta V_N = \Delta V / \Delta V_0$, where ΔV and ΔV_0 are the potential differences between the receiving electrodes (V_{RX2} - V_{RX1}) in the medium and in vacuum, respectively. ΔV_0 being known from vacuum calibrations, the approximate complex permittivity would be directly derived from the value of ΔV_N using Eq. 3. However, this procedure is not entirely satisfactory because its validity relies upon the fact that the injected current is constant and independent of the medium permittivity, which is not strictly the case.

5.2 Self-consistent analysis of the PWA-MIP data

Forward approach. The self-consistent procedure to analyze the PWA-MIP data is illustrated in Fig. 4. It consists in running simulations to predict the value of ΔV for a given ground complex permittivity and instrument geometry. Seven conductors are considered, including the Huygens conductive capsule. These conductors are connected on one side to the electronic network, and on the other side to the medium. The latter is represented by a lumped circuit network computed with the finite element technique, as in Cadène (1995), Simões (2007) and Hamelin et al. (2007). The forward approach gives the forecasted voltage at all electrodes and in particular $\Delta V = V_{RX2} - V_{RX1}$. The expected V_{ADC} at ADC level can then be calculated and normalized by that obtained in vacuum; it is thereafter referred to as $(V_{ADC})_N$.

Inverse procedure. In order to derive the dielectric constant ε_r and the conductivity σ from the measured potential, the forward procedure is repeated for a set of values of ε_r and ε_i, thus producing a chart of forecasted $(V_{ADC})_N$, in the complex plane, made of two families of intersecting curves, one for constant ε_r and one for constant ε_i. Reporting the measured amplitude and phase of $(V_{ADC})_N$ on the chart yields the associated complex permittivity by interpolation (see Fig. 7). There is a bi-univocal relationship between the measured complex voltage and the medium permittivity. Errors can only result from uncertainties on the operation geometry and electric circuitry noise.

The inverse procedure is put into practice once the PWA instrument integrity and attitude after the Huygens landing have been estimated (section 6.1). Practical computing aspects are addressed in section 6.3.
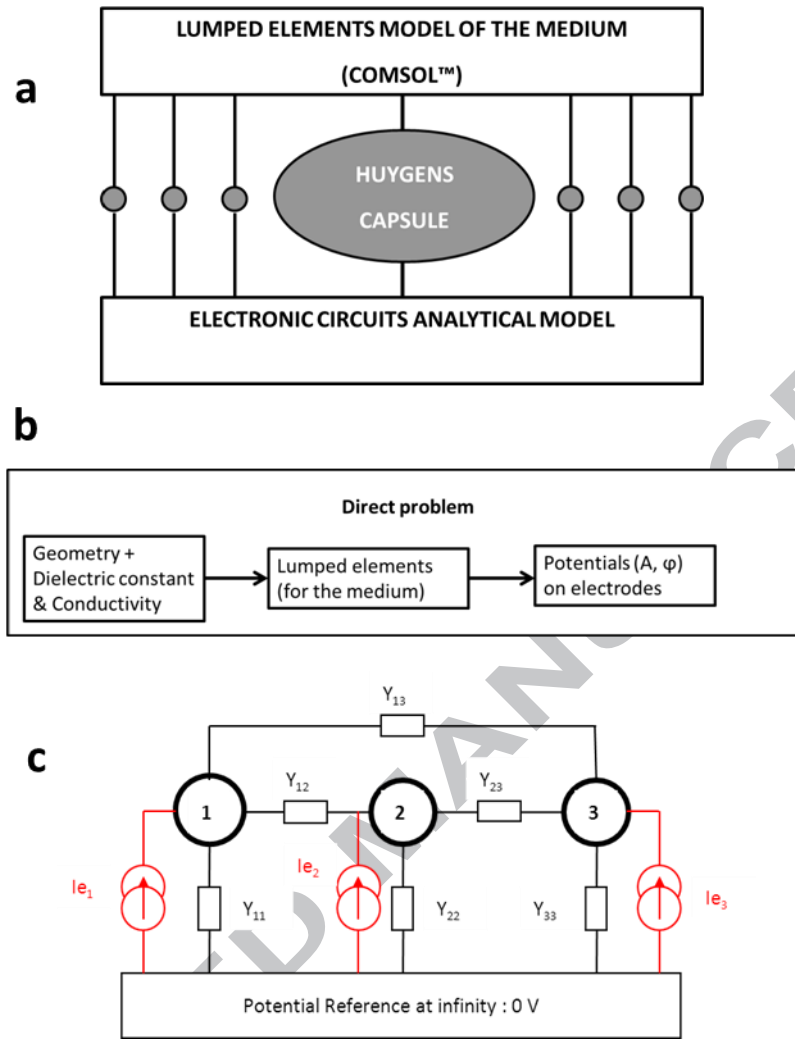
Figure 4. Diagrams illustrating the principle of self-consistent numerical approach: a) Splitting the system into electronic network and the medium. b) Direct problem solving process. c) Template network model in the case of 3 electrodes.

5.3 The capacity-influence matrix: a model of the external circuit made of lumped electronic elements

Theoretical background. A first numerical model was developed by Cadène (1995) to evaluate the influence of the Huygens body on the mutual impedance measurements and to estimate the potential induced at any locations by charges carried by TX electrodes. Our model was developed with COMSOL Multiphysics™ software. It takes into account 7 conductors, namely the 4 electrodes of PWA-MIP, RP1 and RP2, and the Huygens capsule. Further in the paper we write the circuit equations in a matrix form that relates potentials and

currents, using the following subscripts for each of the 7 conductors: 1 for Huygens body, 2 for MIP-TX1, 3 for MIP-TX2, 4 for MIP-RX1, 5 for MIP-RX2, 6 for RP1 and 7 for RP2.

The equivalent electrostatic problem is that of N conductors in vacuum (e.g. Durand, 1966). The charges are related to the potentials through the relation:

$$\mathbf{Q} = [\mathbf{K}]\ \mathbf{V} \tag{5}$$

with $\mathbf{Q} = \{q_1, q_2, ... q_N\}$ and $\mathbf{V} = \{V_1, V_2, ... V_N\}$; q_n and V_n are respectively the charges and potentials of conductor n for n = 1..N. $[\mathbf{K}]$ is the capacitance-influence matrix (with $K_{nn} > 0$ and $K_{mn} < 0$ if m≠n).

In harmonic regime, the current vector $\mathbf{I_e} = \{I_{e1}, I_{e2}, ... I_{eN}\}$ injected in the conductors and the potential vector $\{V_1, V_2, ... V_N\}$ are related by the equation

$$\mathbf{I_e} = i\omega\ [\mathbf{K}]\ \mathbf{V} \tag{6}$$

Let us now define a lumped elements circuit according to the following procedure: each conductor m is linked to the conductor n through the admittance Y_{mn} and to a zero potential reference at infinity through the admittance Y_{mm}. The case of 3 conductors is illustrated in Fig. 4c. The circuit equations with Eq. (6) yields:

$$Y_{mm} = i\omega\ \sum_{n=1}^{7} K_{mn} \tag{7}$$

$$Y_{mn} = -\ i\omega\ K_{mn} \qquad (m \neq n)$$

In vacuum, Y_{mn} are the admittances of elements which capacitances C_{mn0} in vacuum can be computed by solving the Laplace equation with COMSOL Multiphysics™. In a dielectric and conductive medium, each vacuum capacitance C_{mn0} is replaced by a capacitance $\varepsilon_r C_{mn0}$ in parallel with a resistance $R_{mn} = \varepsilon_0/(\sigma C_{mn0})$. All Y_{mn} are therefore proportional to ε^*.

Geometrical model of the Huygens capsule and of the PWA electrodes

For sake of simplicity, the capsule is represented by a body with a cylindrical symmetry around the z axis, which corresponds to the Xp axis in the official Huygens terminology (see Fig. 6). The booms lie in the xz plane (resp. YpXp plane). Rings and disks are not easy to model because they are thin compared to their diameter. They are thus simply replaced by elements with the same capacitance: spheres, or, in the case of RX1 and RX2 that are close to the surface, by cylinders whose height equals the RX diameter, in order to simulate more easily their penetration into the ground. All the model parameters are reported in Table 1.

Name	Geometry	Dimensions	Capacitance [pF]	Model	Coordinates [m]		
					x	y	z
Huygens Probe	See Fig. 1a	ϕ=1.3x0.7m	62.83	simplified: axisymmetric	Origin of coordinates: Bottom of Probe		
TX1	Ring 1.2mm	ϕ=65mm	1.85	sphere r =16.6 mm	0.252	-0.885	-0.070
TX2	Ring 1.2mm	ϕ=65mm	1.85	sphere r =16.6 mm	0.252	0.885	-0.070
RX1	Ring 1.2mm	ϕ=100mm	2.64	cylinder h = 100 mm r =11.4 mm	0.042	-1.043	0
RX2	Ring 1.2mm	ϕ=100mm	2.64	cylinder h = 100 mm r =11.4 mm	0.042	1.043	0
RP1	Disk	ϕ=70mm	2.50	sphere r = 22.8 mm	0.139	-0.811	0.04
RP2	Disk	ϕ=70mm	2.50	sphere r = 22.8 mm	0.139	0.811	0.04

Table 1. Geometrical model of the Huygens Probe and of the PWA electrodes.

Full model with ground interface

A half space of complex permittivity ε^* can be added to the modelled volume. Numerical simulations can then be run to estimate the capacity-influence matrix, or lumped elements admittance matrix, for a set of values of ε^* (forward model as described in Fig. 4b). However, if the electrodes do not intersect the ground plane interface, then the capacity-influence matrix for a given value of ε^* can be simply derived by combining two matrices of real elements (pure capacitors): one obtained for an infinite vacuum environment and another one with a mirror in place of the ground interface (see Annex I). Though this situation is unlikely (the Huygens capsule would have to be resting on cobbles for instance), the solution of this simple case allows testing the validity of numerical simulations separating the geometrical parameters from the constitutive ones.

5.4 The electronic circuits

The medium lumped element circuit is defined by the admittance matrix $i\omega[\mathbf{K_M}]$ ($[\mathbf{K_M}]$ being the medium capacity-influence matrix) and the electronic circuit connected to the electrodes

by the admittance matrix $i\omega[\mathbf{K_E}]$ ($[\mathbf{K_E}]$ being the electronic matrix). The equation of the whole system can be written:

$$\mathbf{I_s} = i\omega \, ([\mathbf{K_M}] + [\mathbf{K_E}]) \, \mathbf{V} \tag{8}$$

where $\mathbf{I_s}$ is the vector of the source currents injected by the circuits and $\mathbf{V}$ the vector of electrode potentials. All the vectors have 7 elements (i.e. the number of conductors) and the matrices are 7x7.

Let us now clarify the elements of Eq. 8 and derive $\mathbf{I_s}$ and the $\mathbf{K_E}$ elements from the electronic circuits characteristics.

A simplified representation of the PWA-MIP analogue circuits (PWA-A board) is shown in Fig. 2b. The PWA-MIP electronics is connected to the transmitting and receiving electrodes though a capacitor of 352 pF. The RP2 electrode is connected to the Huygens electrical ground through a passive circuit (not shown on Fig. 2).

	Gains $(s = 2\,i\,\pi\,f \; ; \; s_{cn} = 2\,\pi\,f_{cn} \; ; \; s_0 = 2\,\pi\,f_0)$	parameters
transmitter filter	$G_{TR} = \dfrac{1}{(s/s_0)^2 - \dfrac{(s/s_0)}{Q_{TR}} + 1}$	$f_0 = 18.286$ kHz $Q_{TR} = 0.5967$
preamplifier	$G_{PA} = \dfrac{\sum_{k=1}^{3} s^k n_k}{\sum_{k=0}^{4} s^k d_k}$	n1= 4.31922e-27 n2= 1.12367e-25 n3= 3.01173e-33 d0= 5.91188e-22 d1= 9.29792e-24 d2= 5.32523e-25 d3= 1.64107e-29 d4= 3.21252e-37
filter F1	$G_{F1} = \left(\dfrac{s}{s + s_{c1}}\right)\left[1 + \dfrac{R_3}{R_2}\dfrac{s}{s_{c2} + (1 + s_{c2}/s_{c3})s + s^2/s_{c3}}\right]$	R3/R2 = 210.53 $f_{c1} = 2.40$ Hz $f_{c2} = 16.75$ Hz $f_{c3} = 7.234$ kHz
filter F2	$G_{F2} = \dfrac{1}{(1 + s/s_c)^2}$	$f_c = 16.389$ kHz

Table 2. Transfer functions of the transmitting and receiving analogic circuits

Transmitter circuit. The transmitter circuit delivers, after amplification, a voltage $V_o = 10$ V that is applied to the electrodes through a 2nd order low pass filter and a coupling capacitor. The circuit that connects the DAC (Digital to Analog Converter) output to the coaxial cable is characterized by the gain G_{TX}, a 3dB cut-off at 15 kHz for a critical frequency of 18.286 kHz and a quality factor of 0.5967 (see Table 2). The gain amplitude decreases slowly at higher frequencies (by a factor of 0.96 at 5760 Hz), but the phase shift is significant (-30.37° at 5760 Hz as shown in Table 3). The value $G_{TX} =1$ at 45 Hz is valid in the atmosphere (Hamelin et al., 2007). The signal is fed through a buffer amplifier and a voltage source V_oG_{TX} is delivered at the output of the PWA-A electronic board that is connected via a coaxial cable to the TX electrode, through a coupling capacitor C_T. A signal to ground leakage capacitor C_S (that includes the input impedance of the operational amplifier and wiring capacitances) connects each TX electrode (conductors 2 and 3) to the "reference ground", that is to the Huygens capsule (conductor 1). Laboratory measurements on spare models give $C_T = 0.425$ pF and $C_S = 0.3$ pF, both within a 20% accuracy (Trautner and Falkner, 2000). These calibration measurements were performed at room temperature. Under frigid Titan conditions, the capacitances of the coupling circuits that lie outside the capsule should decrease due to shrinking.

	45 Hz	90 Hz	360 Hz	1440 Hz	5760 Hz
G_{TX} (dB)	0.0	-0.0001	-0.0014	-0.0219	-0.3746
G_{TX} (°)	0.236	0.473	1.890	7.564	30.372
G_{RX} (dB)	23.1559	23.5006	23.5839	23.0667	16.9741
G_{RX} (°)	25.243	10.397	-10.082	-52.823	-192.418
Rin (GΩ)	0.1795	0.0226	-0.0249	-0.0249	-0.0095
Cin (pF)	0.287	0.288	0.289	0.295	0.335

Table 3.Input impedance and gains of the transmitting and receiving circuits

As an example, the nodal equation at the TX1 transmitter circuit (conductor 2) can be written:

$$I_S(2) = i\,\omega\,V_o\,G_{TR}\,C_T = i\,\omega\,[V(2) - V(1)]\,(C_T + C_S) + i\,\omega \sum_{n=1}^{7} V(n)\,K_M(2,n) \quad (9)$$

which implies that: $K_E(2,2) = - K_E(2,1) = - K_E(1,2) = C_T + C_S$ (symmetrical matrix) and a term $(C_T + C_S)$ in $K_E(1,1)$ (see Table 4). The source term $I_S(3)$ relative to TX2 is developed in

the same way as for TX1. Since the TX1 and TX2 circuits are identical, but with opposite signs for the voltage source, $I_S(3) = -I_S(2)$. All other components of I_S are equal to zero because of the absence of any source and because $I_S(1) = I_S(2) + I_S(3) = 0$.

The derived matrix coefficients are $K_E(3,3) = -K_E(3,1) = -K_E(1,3) = C_T + C_S$, and the term to be included in $K_E(1,1)$ is $(C_T + C_S)$ (see Table 4).

We recall that the potential reference in the simulations is zero at infinity while the potential of the Huygens capsule differs from zero. Accordingly, all simulated electrode potentials have to be shifted by the potential of the reference Huygens capsule before any comparison between measurements and simulations.

Receiver circuit. The receiver circuit includes, for each boom, a coupling capacitor housed inside the boom itself, a preamplifier in the HASI-I box, inside the capsule, as well as a differential amplifier and several circuits for accommodating the signals to the ADC input, on the PWA-A board. The parameters, gain and input impedance have been estimated from the nominal component values or derived from calibration measurements.

	1 (HUY)	2 (TX1)	3(TX2)	4(RX1)	5 (RX2)	6(RP1)	7(RP2)
1 (HUY)	$2(C_T+C_S)$ $+2\,C^*_{in}$ $+C_{RP}$	$-(C_T+C_S)$	$-(C_T+C_S)$	$-C^*_{in}$	$-C^*_{in}$	0	$-C_{RP}$
2 (TX1)	$-(C_T+C_S)$	C_T+C_S	0	0	0	0	0
3 (TX2)	$-(C_T+C_S)$	0	C_T+C_S	0	0	0	0
4 (RX1)	$-C^*_{in}$	0	0	C^*_{in}	0	0	0
5 (RX2)	$-C^*_{in}$	0	0	0	C^*_{in}	0	0
6 (RP1)	0	0	0	0	0	0	0
7 (RP2)	$-C_{RP}$	0	0	0	0	0	C_{RP}

Table 4. Electronic matrix **[K_E]**

The outputs of the two HASI-I1 and HASI-I2 MIP preamplifiers are connected to a differential amplifier in PWA-A. This signal is then fed into the ADC through two filters whose gains G_{F1} and G_{F2} are estimated from the components listed in Table 2.

The preamplifiers represent the most sensitive parts of the receiver for two reasons. First, they are connected to the electrodes through very small capacitors, and stray capacitances that

cannot be evaluated with accuracy. Second, preamplifiers and PWA-A board are located inside the capsule that is heated with radioactive elements, while the coupling capacitors lie outside at ~ -180 °C. Such a configuration is impossible to simulate in laboratory. The preamplifiers have been calibrated in two experimental conditions: (1) HASI-I MIP preamplifiers and booms at room temperature, and (2) HASI-I MIP preamplifiers at room temperature and booms with coupling circuits at ~ -180 °C (liquid nitrogen). The construction of an accurate analytical model supported with calibration data, is detailed in Annex II. For Titan's environment, the G_{PA} gain analytic expression is shown in Table 2. The numerical values of gain and input impedance components, R_{in} and C_{in}, are shown in Table 3.

The complete calibration data set (electrodes + preamplifiers + PWA-A board) at room temperature is found in Jernej and Falkner (2004).

The derived matrix coefficients for conductors 4 (MIP-RX1) and 5 (MIP-RX2) are:

$K_E(4,4) = K_E(5,5) = - K_E(4,1) = - K_E(1,4) = - K_E(5,1) = - K_E(1,5) = C_{in}–i/\omega R_{in}$, and their counterpart in $K_E(1,1)$ is 2 $(C_{in}–i/\omega R_{in})$, as shown in Table 4.

RP electrodes and circuits. The RP1 electrode can be regarded as a floating conductor, but RP2 is connected to the Huygens capsule by a capacitor C_{RP} =352 pF hence:

$K_E(7,7) = - K_E(1,7) = - K_E(7,1) = C_{RP}$, and the addition term C_{RP} in $K_E(1,1)$ (see Table 4).

6. The Titan PWA-MIP data analysis

In this section, we apply the analysis approach described in section 5 to the data collected on Titan's surface. We first determine the possible configurations of operation of PWA-MIP at the surface of Titan in order to realistically simulate the medium capacity-influence matrix K_M (section 6.1). We then proceed to some adjustment on the electronic matrix K_E based on vacuum calibration at 45 Hz (section 6.2). Measurements collected at 45 Hz (section 6.3) and higher frequencies (section 6.4) are then compared to the results of our numerical model in order to infer the ground complex permittivity and reliable associated uncertainty.

6.1 Derivation of the geometry of PWA-MIP operations on Titan from the Huygens landing scenario

The Huygens Probe survived the landing but did not return clear information about the integrity of the booms and the final configuration of the quadrupole on the surface.

In its nominal attitude, the Huygens Probe is standing upright on a flat surface; the TX electrodes remain above the interface and the lower parts of the RX electrode rims are buried, a few mm below the surface. In reality, the surface of the ground was probably altered by the impact, and the contact area between the Huygens capsule and the ground, as well as the location of the MIP electrodes with respect to the interface, depend on the lander penetration depth and attitude. Knowing the possible geometry of operation of PWA-HASI is crucial to analyze the data acquired at Titan's surface.

Grard et al. (2006) first addressed the effect of the geometry of operation on the estimation of the ground complex permittivity but with a preliminary scenario for the Huygens landing. Grard et al. (2006) also noted an abrupt change of permittivity, about 11 minutes after landing, without providing an explanation for it. Since then, thanks to a synergy between various Huygens experiments, such as HASI-ACC (accelerometers), DISR (images) SSP (attitude), it has been possible to reconstruct the scenario of the landing (Bettanini et al., 2008; Schröder et al., 2012). A model of the dynamics of the landing is illustrated in Fig. 13 of Schröder et al. (2012). The Huygens Probe hits the ground with a vertical velocity of 4.60 m/s digging a 12.2 cm depression. It then bounces out with a restitution coefficient allowing it to reach the original ground level. With a horizontal velocity of ~1 m/s, the Huygens then skids on the surface and stops ~5 s after the impact, with perhaps some slight wobbling for another few seconds.

Huygens probe dynamics and resting position

In order to better understand the possible attitude of the Huygens lander at its final position, we developed a simple model to derive the strength of the surface material from the depth of penetration of the lander. The bottom dome of the Huygens Probe is spherical, with a radius $R=1.215$ m. Assuming a completely rigid capsule and, for the ground reaction force, a solid

friction proportional to the contact surface with the ground ($S \sim 2\pi Rh$, where h is the penetration depth at time t after touch down) and neglecting Titan's gravity, the equation of motion is:

$$h'' = -\Omega^2 \ h \tag{10}$$

where h'' is the second time derivative of h, $\Omega^2 = 2\pi RK/M$, where M is the mass of the Huygens Probe and K the mechanical resistance of the material (N/m^2). Integrations of the equation of motion then lead to:

$$h' = v_0 - h_0 \ \Omega(1 - \cos \Omega t) \quad \text{and} \quad h = (v_0 - \Omega \ h_0) \ t + h_0 \ \sin \Omega t \tag{11}$$

where v_0 is the vertical landing velocity at $t = 0$ and h_0 the depth of the penetration. We thus infer for K a value of 34 kPa, a maximum deceleration of 160 m/s^2 and a penetration time of 44 ms. We note that the retrieved value of K is comparable to that of ~50 kPa found by Bettanini et al. (2008).

After this first impact, the Huygens Probe likely had no more vertical velocity and skidded on the surface before stopping in a field covered with pebbles and cobbles of diameter ~2-20 cm, as seen in the DISR images (Tomasko et al. 2005). If the surface on which the Huygens Probe landed is flat, it then must have penetrated it by less than a 1 mm (given the inferred value of K). However, if the Huygens Probe ended on pebbles, it must be standing slightly above the ground level and this needs to be accounted for in our numerical simulations all the more as it has implications on the quality of the PWA-MIP electrode-ground contact.

Additional geometric information on the resting position of Huygens Probe from parallax in the camera system, and the sharpness of focus of features on the ground indicates (Karkoschka et al., 2007) that the camera window was 48±2cm above the ground – essentially equivalent to the base of the probe being 1±2cm above ground level. This is also consistent with a weaker but entirely independent constraint derived from the multipath interference pattern seen in the probe radio signal, which indicates the phase center of the antenna to be 75±5cm above the ground, or that the base of the probe was 1±5cm above ground level (Pérez-Ayúcar et al., 2006).

We therefore decided to study two extreme configurations:

(1) the Huygens capsule is sitting on pebbles, at 3 cm above the ground,

(2) the bottom of the Huygens capsule has penetrated a smooth and flat surface by 1 cm.

Booms dynamics and integrity

An interrelated problem is the behaviour of the booms and electrodes during landing. There is little doubt that the tip of the booms and the RX rings stroke and penetrated the ground as the capsule itself during the first impact, and that the relatively flexible fiber-glass booms have been momentarily deformed. However, landing with a rotation rate of ~1 rpm corresponds to a rotational motion of only ~4 mm at the tip of the booms during the deceleration phase of ~44 ms. As a consequence, the booms were most likely not twisted when sunk such a short time into the ground. Nevertheless, it is useful to know whether the capsule continued to rotate after jumping out of the depression it created.

In continuation of the model previously described, we assume that the rotation is damped by solid rotational friction at the contact between the capsule and the ground. The coefficient of friction η is the ratio between the tangential and the normal force for an infinitesimal surface of contact; it is estimated to be 0.4 ± 0.1 (Schröder et al., 2012). The resistive torque Γ for a ring of radius r and an infinitesimal size dr is $d\Gamma=2\pi\eta Kr^2$. For a penetration depth h the contact area is close to a disk of radius $a=(2Rh)^{1/2}$ and the related torque is $\Gamma=(2\pi/3)\eta Ka^3$. The dynamic equation of the capsule rotation is then:

$$\omega'_H = \alpha h^{3/2} \quad \text{with} \quad \alpha = \eta\ 2^{5/2}\frac{\pi}{3}\ R^{3/2}\frac{K}{I_M} \tag{12}$$

where ω_H is the rotation rate of the capsule and I_M is the moment of inertia of the capsule, namely 24.5 kg.m^2 (Lebleu, 2005). The equation has been solved numerically for several values of η and the results are displayed in Fig. 5. For all values of η in the range 0.4 ± 0.1, ω_H vanishes before reaching the bottom of the depression. This study thus shows that the capsule rotation had completely stopped before the end of the impact, which strongly speaks in favour of the integrity of the booms.
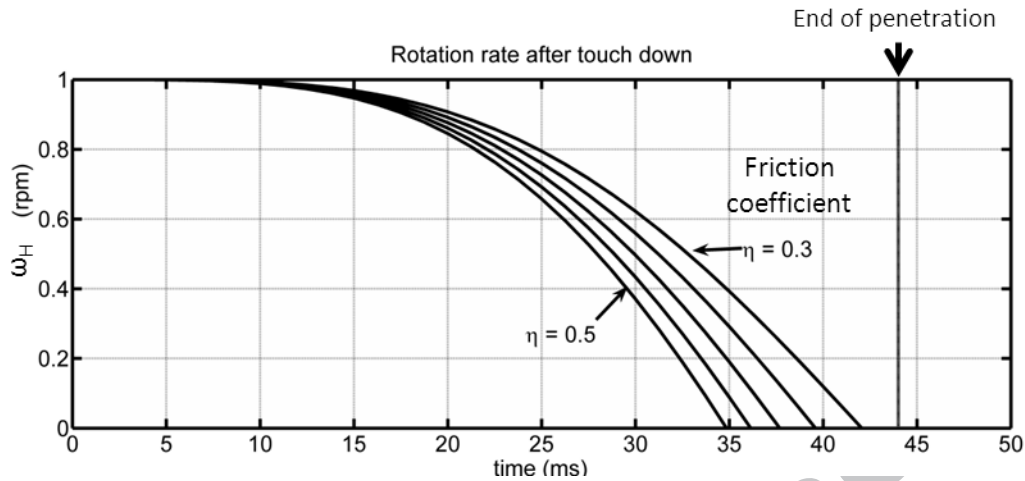
Figure 5. Capsule rotation rate (ω_H) vs. time during the first impact for several friction factors (η). The vertical black line at 44 ms indicates the end of the penetration period as inferred in section 6.1

Moreover, after skidding on the surface, the Huygens Probe was tilted towards the DISR pointing direction, almost perpendicularly to the boom direction (Yp axis). The booms are flexible and the RX electrodes may have not penetrated again the ground. However, since there is no way to know whether the RX electrodes are partially buried or not at Huygens final resting position, we decided to consider the two extreme configurations mentioned previously (capsule 3 cm above and 1 cm below the ground) in two cases:

(1) without tilt

(2) with tilt, i.e., with one RX electrode above the surface and the other one slightly inserted into the ground.

The four study configurations, labelled A, B, C, D are shown in Fig. 6; they should encompass the actual configuration of operation of PWA-MIP at Titan's surface.
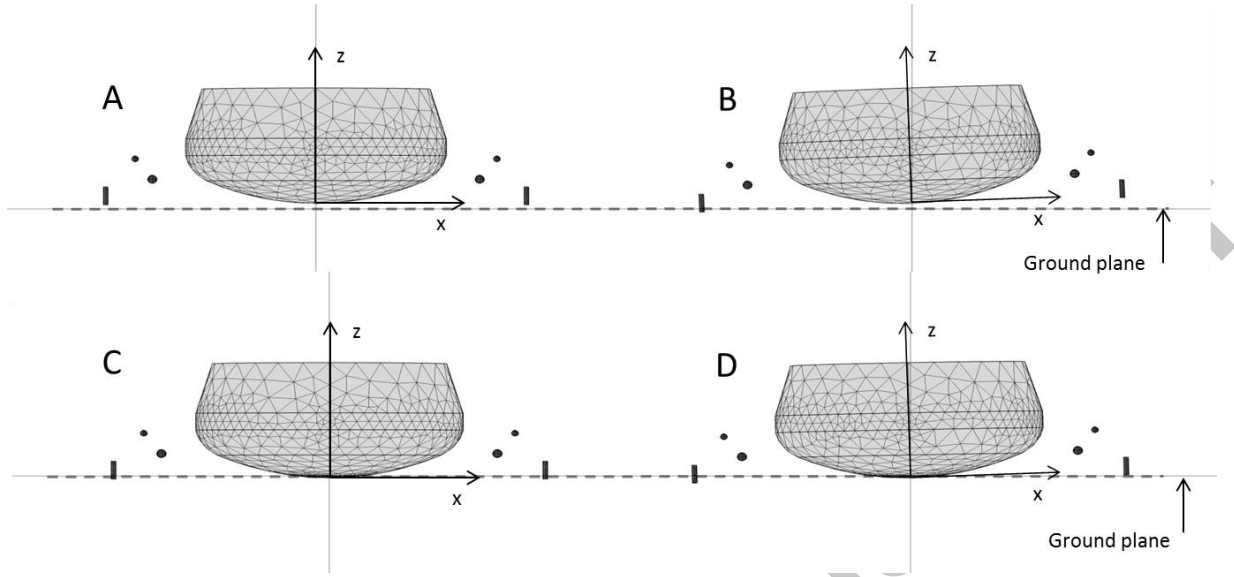
Figure 6. Four possible model configurations: capsule on pebbles, above the ground (A and B), or slightly sunk into the ground (C and D), in an upright position (A and C) or tilted, with one RX electrode above the ground (B and D).

6.2 Adjustment of the electronic model using the 45 Hz pseudo-vacuum calibration during the Huygens descent

The capacity-influence medium matrix $[K_{M0}]$ for the capsule in vacuum is computed using the COMSOL Multiphysics™ software for the geometrical model of Huygens as defined in Table 1. The voltage at all electrodes is derived from Eq. 8 and from parameters of Table 4:

$$\mathbf{V} = V_0 \; \boldsymbol{G_{TR}} \; C_T \; \left[[K_{M0}] + [K_E]\right]^{-1} \; \mathbf{U_I} \tag{13}$$

where $\mathbf{U_I}$ is a vector of 7 zero elements except 1 for U(2) and -1 for U(3) (this corresponding to the current injected between the two TX electrodes).

We here note that the vacuum calibrations of PWA-MIP with the Huygens Probe performed before flight are not exploitable due to an inappropriate testing environment (vicinity of cooling systems and electromagnetic noise). As a consequence, our reference is the set of measurements performed just before landing, during the descent of the Probe. As discussed in section 3.1, these measurements were performed in a neutral atmosphere that can be

considered as vacuum in a quasi-static regime, even though some atmospheric effects may exist in the radio-frequency or optical domains.

At 45 Hz, using the values $C_T = 0.425$ pF and $C_S = 0.3$ pF for the TX coupling and stray capacitors (see section 5.3), the predicted voltage amplitude is $|V_{ADC}| = 1.790$ V with a phase of $-153.44°$ with respect to the phase of V_0 (at DAC level), while the measured values during descent was $|V_{ADC}| = 1.842$ V with a phase of $-158.04°$ (see section 3.1 and the green dots in Fig. 3a).

Coupling capacitor adjustment. There are several causes for the discrepancy between the measurements and the model: lack of precision of the simplified geometrical model, thermal shrinkage of the capsule structure and of components such as the coupling capacitors (of the order of 0.5-1% for aluminium and polyimide at Titan temperature). However, these causes should have a much weaker effect than the ~20% uncertainty on the values of C_T and C_S. In particular, the model is very sensitive to C_T and we note that taking $C_T = 0.441$ pF instead of 0.425 pF gives the right amplitude $|V_{ADC}| = 1.842$ V. In the remainder of the paper, we therefore consider: $C_T = 0.441$ pF. Nevertheless, this value does not allow reducing the difference of $4.60°$ between the phase predicted by the model and the measurements.

Phase correction. A phase shift of $4.60°$ is not negligible for the evaluation of the conductivity that is dominantly controlled by the phase of the measured voltage. There are uncertainties in calibrations and models, possibly due slight modifications of the electronics during the long interplanetary journey of the Cassini probe. It is possible that the characteristics of the instrument have evolved during the Cassini cruise. In particular, the coupling circuits are embedded into the booms and thus remained outside the metallic shield offered by the capsule. As a consequence, they were more exposed to radiations than the HASI-I components, and the polyimide material they are made of could have become slightly conductive. A dedicated study could be envisaged but, for this paper, we decide to take the last atmospheric measurements as a reference and simply apply a $4.60°$ correction to the measured phase. We emphasize that, in the single 45 Hz case, a correction by a complex factor would produce the same results. Nevertheless our aim is to obtain a more accurate value for the coupling capacitor which is used in the electronic model, in order to apply a correction that would be suitable over the whole frequency range of the instrument.

6.3 PWA-MIP measurements and results at 45 Hz

The calibration of the instrument in a pseudo-vacuum environment was only performed at 45 Hz. For that frequency, normalized values of V_{ADC} that lead to complex permittivities (see section 3.1) can be obtained without additional hypotheses. This is the reason why the analysis of the measurements acquired at 45 Hz is reported first. Results derived from measurements at higher frequencies are presented in section 6.4.

Once the vacuum voltage reference is found, we have access to the normalized voltages $(V_{ADC})_N$ and are able to compare the PWA-MIP measurements with predictions from numerical simulations. In Fig. 7, the measured normalized voltages are plotted in the complex plane for the 4 tested geometrical configurations of operation (see section 6.1), separating measurements acquired before (Fig. 7a) and after (Fig. 7b) ~11 min after landing (mission time: t=9539 s) where Grard et al. (2006) reported a sudden change. The complex permittivity of the ground can then be inferred from the position of the data points in the charts obtained by numerical simulations repeating the forward procedure for a grid of ε_r and ε_i values relevant to Titan's surface expected composition. The grid is extended from any realistic pairs of (ε_r, ε_i) values till incorporating in the results domain all experimental values of $(V_{ADC})_N$. In the case of geometry A, for which none of the 7 electrodes crosses the ground interface, only one COMSOL simulation matrix is needed for the whole grid (with a perfect conductor at the interface, as shown in annex I), whereas for all other cases B,C,D, a matrix calculation is needed for each point of the grid. In these cases the parameters of the COMSOL model are adjusted carefully to describe the interface vicinity. More specifically, we used values of ε_r in the range 1.8 to 3.2 with step 0.1, and values of ε_i in the range 0 to 0.6 with the same step 0.1. On a PC one grid point calculation takes about 3, 20 and 25 mn for cases B, C and D respectively.
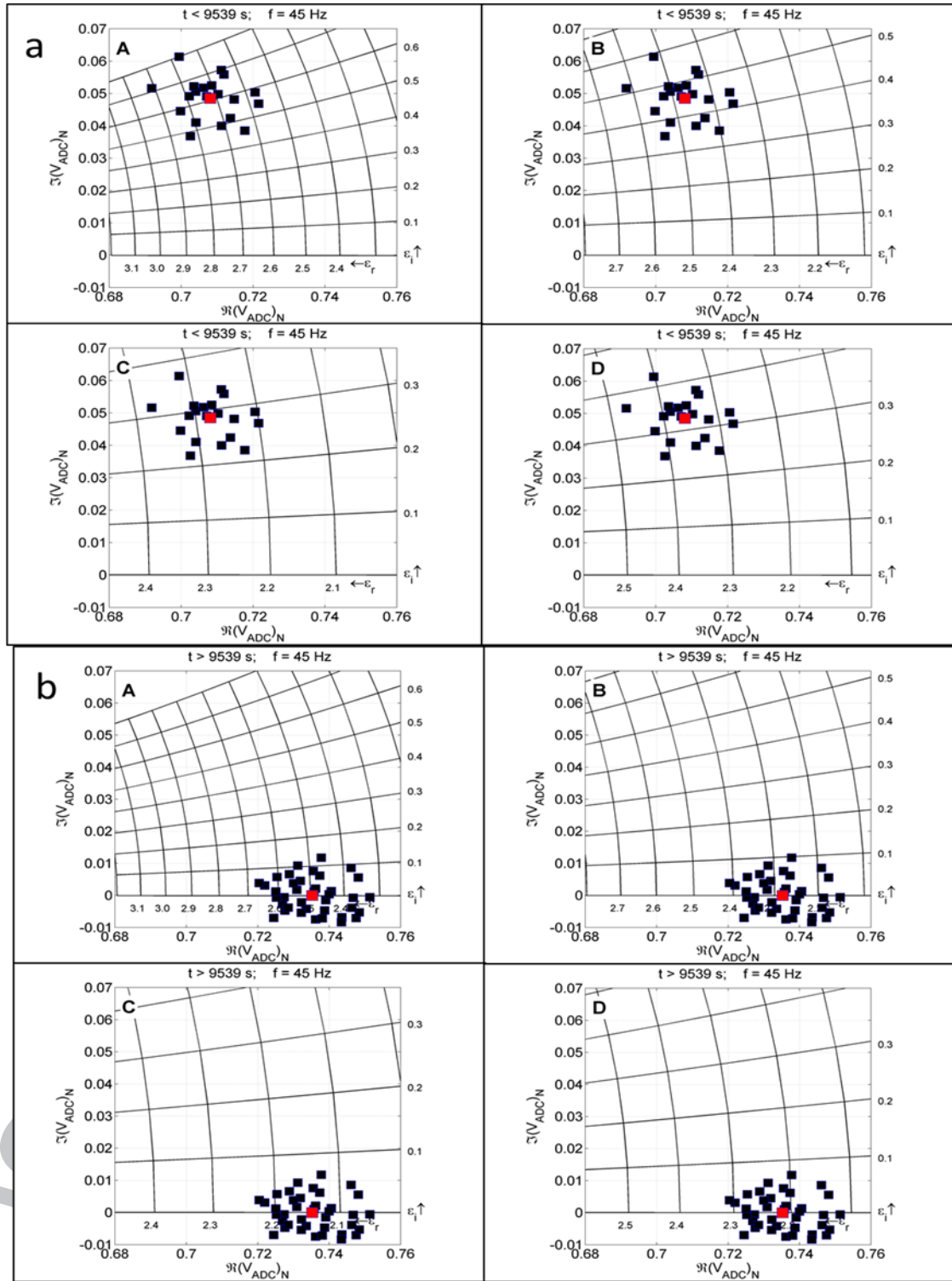
Figure 7. Analysis of the PWA-MIP data collected at 45 Hz on the surface of Titan. The panels show the vacuum-normalized voltages $(V_{ADC})_N$ in the complex plane (square dots) for the four geometries defined in section 6.1, superimposed on grids that give the complex permittivity $(\varepsilon_r, \varepsilon_i)$ for each PWA-MIP measurement. The red square represents the mean of the measurements, a) for $t < 9539$ s and b) for the $t > 9539$ s.

The left panels correspond to geometries A and C for which the Huygens capsule is horizontal (i.e., not tilted, see Fig. 6). The red squares represent the average of the measured normalized complex voltages. There is a significant difference between the value of the ground complex permittivity of ~2.7+0.6i obtained for case A (3 cm levitation) and of ~2.3+0.3i obtained for case C (1 cm insertion). In comparison, there is less difference between case B (3 cm levitation, tilted) with an inferred complex permittivity of ~2.5+0.4i, and case D (1 cm insertion, tilted) with ~2.35+0.3i, for which at least one RX electrode is inserted into the ground.

We therefore conclude that the ground complex permittivity derivation from PWA-MIP is mostly sensitive to the height of the electrodes above the ground interface. Upper panels of Fig. 8 summarize the results (red triangles) and their dispersion (red dashed circles) in the normalized permittivity complex plane. For example, both the dielectric constant and conductivity may be overestimated if the Huygens capsule elevation is assumed to be higher than it is in reality. Fig. 8 also clearly shows that the uncertainty related to the position and attitude of the capsule is greater than the dispersion of the measurements.

Assuming that four geometrical configurations A, B, C and D encompass the actual configuration of operation of PWA-MIP, the projection of the cloud of data points on the axes defines the possible ranges of ε_r and ε_i. For t<9539 s (Fig. 8, top-left), we find: ε_r=2.55±0.35 and ε_i=0.50±0.30, i.e. a conductivity of 1.25±0.75 nS/m. For t>9539 s (Fig. 8, top-right), the results are: ε_r=2.35±0.30 and ε_i=0.0±0.1. Obviously, the imaginary part ε_i cannot be negative and we can write that σ=0 nS/m or, more precisely, that the conductivity value is below the measurement threshold corresponding to the last atmospheric measurements. This unexpected result is neither an artefact nor the consequence of an instrument failure, since the dielectric constant (real part) does not show any significant change. It is further discussed in section 7 as well as the possible composition of Titan's surface at the Huygens landing site based on its complex permittivity.
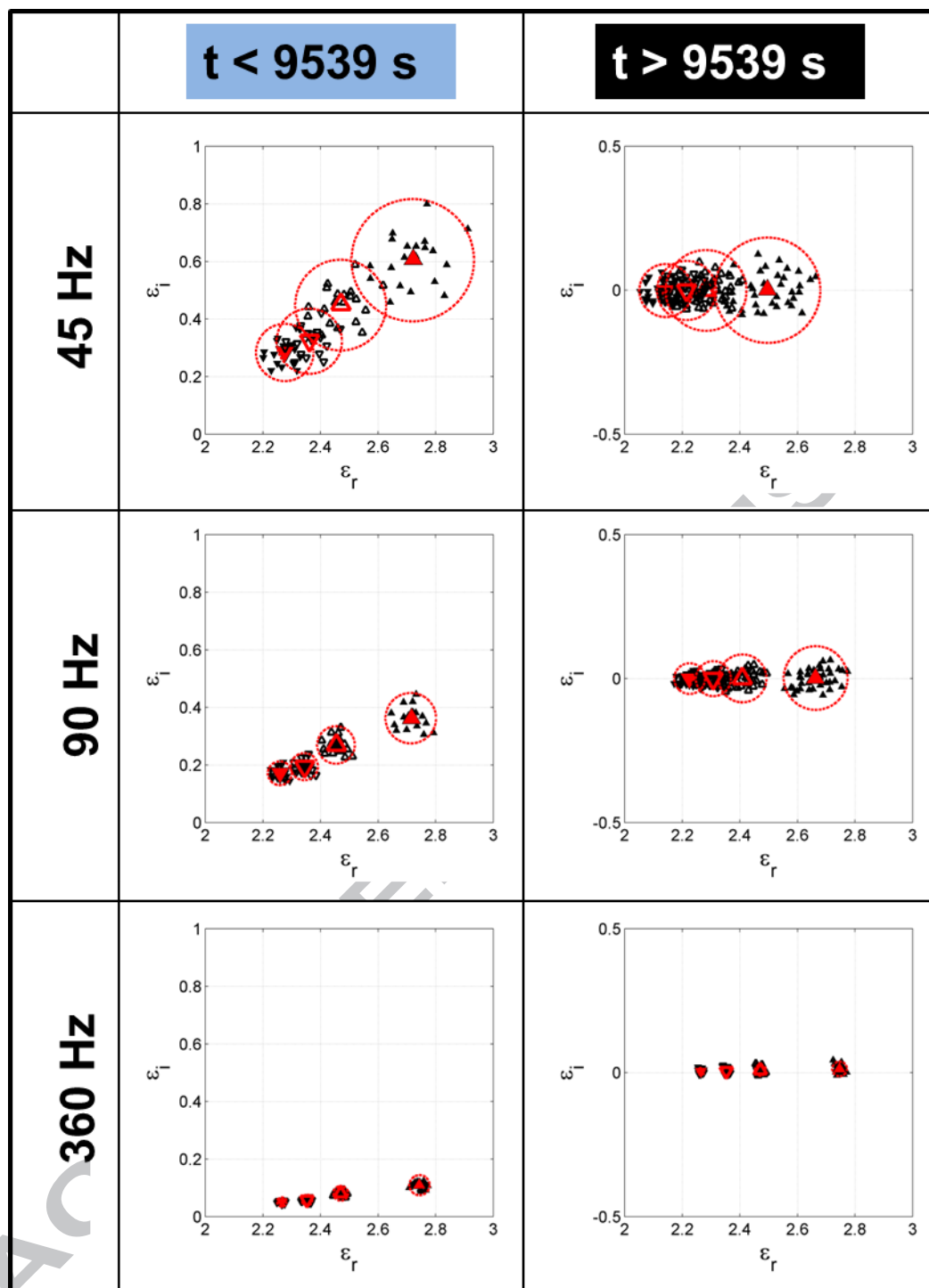
Figure 8. Summary of the complex permittivity deduced from the charts for all geometries, namely A (full upward triangles), B (empty upward triangles), C (full downward triangles) and D (empty downward triangles). The red triangles show the mean values for each geometry and the red circles indicate the experimental dispersion (2 σ). Left panels are for t < 9539 s and right panels are for t > 9539 s. From top to bottom: frequencies 45, 90 and 360 Hz.

6.4 PWA-MIP measurements and results at higher frequencies

There is no vacuum reference at frequencies higher than 45 Hz; the calibration of these data then relies on the analytical model of the electronic circuit (see section 5.4 and Table 2). Yet, the ratio of the voltage amplitudes measured on the Titan surface at 1440 Hz and 5760 Hz differ by about ~3 dB from that given by this model, which cannot be ascribed to a frequency dependence of the ground permittivity. Indeed, the dielectric constant is influenced by the possible presence of polar molecules as H_2O (NH_3 which has a similar dipolar moment is not detected at the surface), but the polarization effects vanish at low temperatures. More specifically, in the case of pure water ice the dielectric constant can be written as $\varepsilon_r = \varepsilon_\infty + (\varepsilon_s - \varepsilon_\infty)/(1 + \omega^2\tau^2)$ where ε_s and ε_∞ are the static and infinite frequency limits of ε_r (see e.g. Petrenko et al., 1999; Eisenberg and Kauzmann, 2005). The value of τ at the temperature of Titan's surface, 94 K, can be estimated by extrapolation from Kawada (1978) to be about 10^5 s. As a consequence, the dielectric constant of pure water ice is strictly equal to $\varepsilon_\infty \sim 3.15$ in the PWA-MIP frequency range, at such a low temperature (supported by laboratory data shown in Mattei et al., 2014, despite of an increasing error bar at low frequencies). Furthermore, the case of mixtures of lunar regolith filled with water ice has been investigated in laboratory by Alvarez, 1973 who showed that the dielectric constant at 100 K of a sample filled with 9% water ice should vary by only about 60% between 50 and 5000 Hz, in agreement with a Cole-Cole theoretical model. Extrapolating the 45 Hz vacuum reference model leads to unrealistic complex permittivity values, at least at 5760 Hz. This anomaly – together with the unexplained phase shift at 45 Hz - probably results from a drift of the amplifier characteristics, possibly due capacitor losses induced by radiations during the Cassini cruise. We therefore discard the measurements performed at the two highest frequencies, namely 1440 and 5760 Hz but keep the measurements collected at 90 Hz and 360 Hz.

Moreover, in absence of vacuum calibration at high frequencies, we make the assumption that the ground conductivity is zero for t>9539 s, as was found for 45 Hz. This assumption provides a reference for the phase of the measured voltages at 90 Hz and 360 Hz while the reference for the amplitude is given by the analytical formulas.

The two middle panels of Fig. 8 show the permittivity in the complex plane at 90 Hz, before and after t=9539 s. The inferred dielectric constant ε_r lies in the range 2.20–2.80 for both

sequences.The range for ε_i is 0.15-0.45 (corresponding to conductivity values in the range 0.75–2.0 nS/m) for t<9539 s. The lower right panel shows the 360 Hz results with ε_r in the range 2.25–2.75 and ε_i in the range 0.04-0.13. At 90 Hz, and even more at 360 Hz, the results are dependent on the landing geometry. As mentioned before, at Titan's surface temperature the dielectric properties of the ground are expected to vary only slightly with frequency and these results nicely support the values found at 45 Hz. The 45, 90 and 360 Hz results are summarized in Fig. 9. They are discussed in terms of composition in section 7.
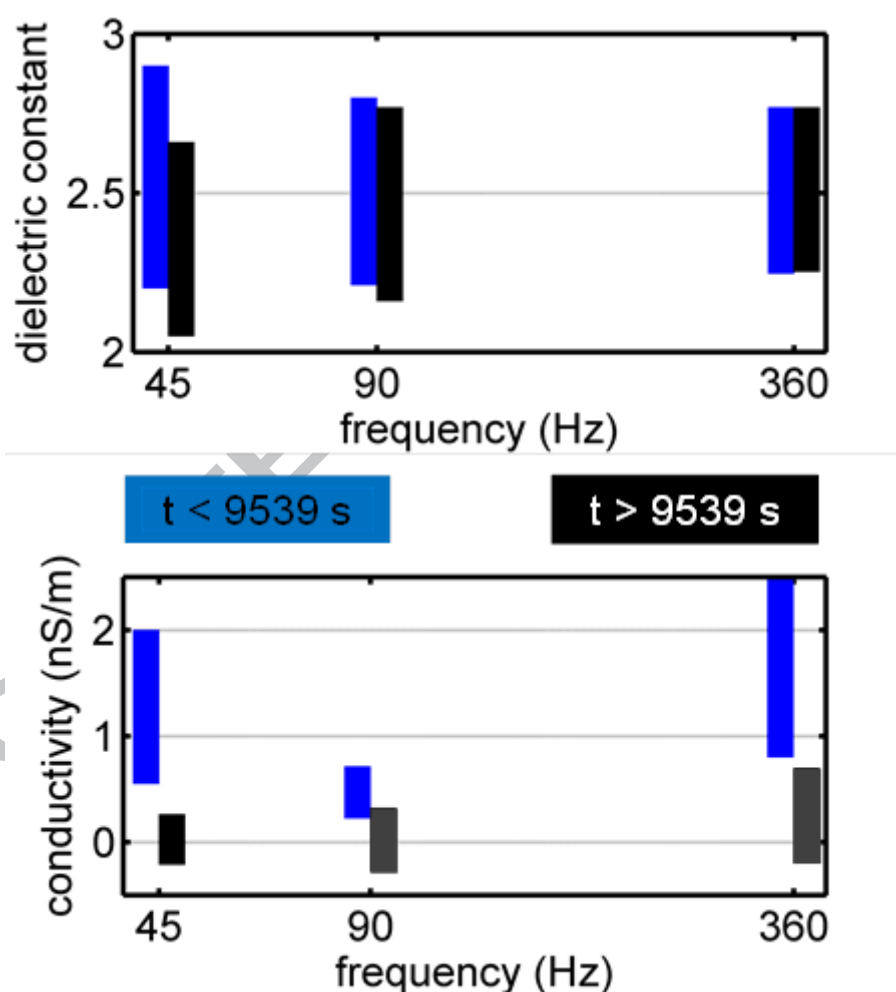

Figure 9. Summary of the results for 45, 90 and 360 Hz. Upper panel: the bars indicate the range covered at each frequency by the dielectric constant for all geometries; blue left bar t < 9539 s; right black bar t > 9539 s. Lower panel: same as above for the conductivity (at 45

Hz, well calibrated measurements of conductivity; at 90 and 360 Hz and for t > 9539 s: mean conductivity forced to zero and gray bars are representative of measurement dispersion).

7. Titan's surface composition and the 9539 s event

7.1 Titan's surface composition

We find that the surface of Titan at the landing site has a dielectric constant of 2.5±0.3 and a conductivity 1.2±0.6 nS/m. Though not very constraining on the composition, these values are consistent with the complex permittivity of materials expected on Titan. In particular, the inferred dielectric constant is close to that of solid organics (2-2.4) as measured in laboratory at a higher a frequency but low temperature (77 K) by Paillou et al. (2008). Slightly higher values (2.85-2.95) were found for nitrile compounds, which are also plausible candidates for Titan's surface, at low frequencies (100 Hz) (Le Gall et al., 2015, submitted). The inferred dielectric constant is compatible with the presence of liquid methane or ethane (<2.0, Mitchell et al., 2015) in the pores of the near-surface. Likewise, although the inferred dielectric constant is not compatible with solid compacted water ice as a major compound of the near-surface of the Huygens landing site (see §6.4), the presence of water ice cannot be ruled out either in small to moderate abundance or in a porous form. In that respect such ambiguous conclusion is not conflicting with the current observations of Griffits et al. 2003 which detected water ice from telescope infrared spectroscopy measurements, and of Clark et al. 2010 suggesting from Cassini measurements that water ice is not a major component of the exposed surface material. With well-calibrated MIP measurements at the five frequencies it would have been possible to derive some Cole-Cole models from the results but unfortunately the relatively large error bars on the only three validated frequencies erode the value of such analysis. The implications of the inferred conductivity value are discussed in section 7.2.

Overall, the PWA-MIP results speak in favour of a photochemistry origin for the first meter of Titan's surface at the Huygens landing site. Though its bulk crust is believed to be made of water ice (e.g. Tobie et al., 2005), the complex atmospheric photochemistry of Titan produces a wealth of organic molecules that are eventually deposited at the surface, in the form of a

sedimentary layer. Our interpretation of the PWA-MIP results is also supported by the idea that the Huygens Probe landed on a dry riverbed (Tomasko et al., 2005).

7.2 The 9539 s event

The second key outcome of this refined analysis of the PWA-MIP data is the interpretation of the sudden change observed about 11 min after the Huygens landing. It emerges from the 45 Hz data that the apparent ground conductivity suddenly dropped at t=9539 s below the measurement threshold. Our investigation of this phenomenon rules out any cause due to hardware failure. We are therefore left with the challenge of proposing a plausible explanation for this event.
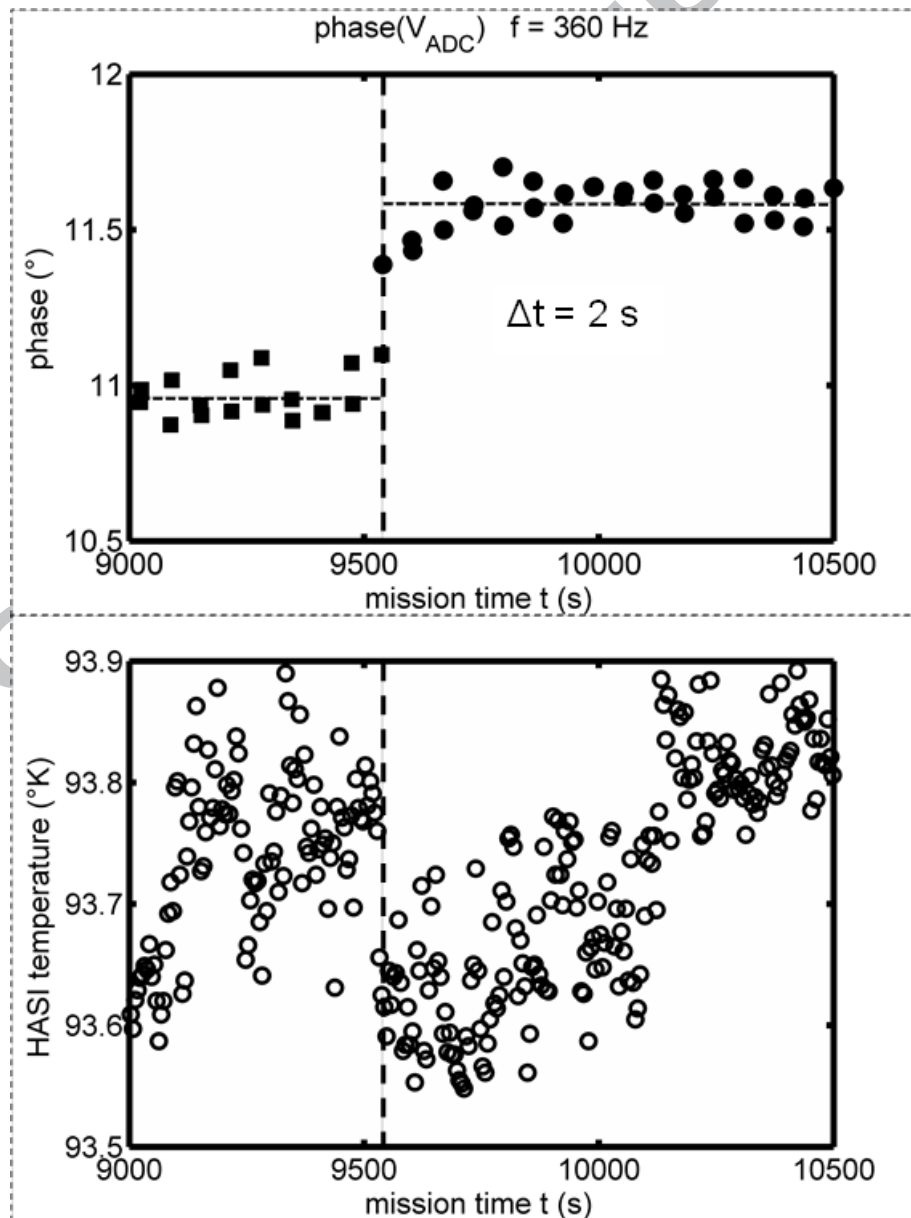
Figure 10. Simultaneous discontinuities in the PWA-MIP V_{ADC} phase at 360 Hz and the HASI temperature are observed at around 9539 s.

Other Huygens data acquired around 9539 s

There is no indication of motion around 9539 s in the data acquired by the SSP tilt sensor, the accelerometer (which were both recording every second) or in the images acquired periodically by the DISR camera. The 9539 s event thus cannot be ascribed to a change in the probe position or attitude. The GCMS instrument did detect a continuous increase of the ambient atmospheric content of methane after landing, likely a consequence of outgassing of the ground heated by the Huygens probe (Niemann et al., 2010, see also Lorenz et al., 2014), but this evolution was continuous and shows no sudden change at 9539 s. The most relevant observation for the 9359 s event was obtained by the HASI temperature sensor: a 0.2 K drop of temperature was measured at exactly the same time (see Fig. 10). Since the HASI temperature sensors are ~1 m away from the PWA-MIP electrodes, the detected event must be relatively large scale. While an abrupt change of the electrical properties of the ground volume under the Huygens Probe is excluded, a change in a superficial layer could explain these observations.

The outgassing scenario

Bubbles of gas released from beneath the probe might explain the observed temperature jump. Simple thermal conductivity considerations suggest that heat from the probe could, in 11 minutes, alter the surface material temperature down to a depth of ~10 cm. If such a heat leak raised the vapour pressure of volatile materials confined in the subsurface to the point that they broke through some obstruction and boiled away, then the relatively warm gas would briefly perturb the environment, and the removal of material from the subsurface would decrease the overall dielectric constant.

As for the conductivity, it is worth considering that tholins have much higher electrical losses (ε_i ~10^{-2} vs 10^{-4}-10^{-3} for simple hydrocarbons – Paillou et al. 2008). Some polymers (notably polyacetylene) have semiconductor properties (e.g. Thompson and Squyres, 1990) and may be present in Titan surface materials. If the volatile material suddenly released at 9539 s were itself responsible for the surface conductivity, or if it blew away some fine-grained material that was conductive (perhaps the fluffy deposit interpreted from the penetrometer (Atkinson et

al., 2010) and optical data (Schröder et al., 2012) may have had a polyacetylene or similar component) then the observed changes may be at least qualitatively explained. It is of note that the measured dielectric constant of polyacetylene is quite high (~5, Thompson and Squyres, 1990) so that the removal of only a small amount (typically ~1 cm superficial layer) of this material would cause a measureable drop in the overall apparent dielectric constant of the subsurface. The quantitative value of AC conductivity of polyacetylene quoted by Thompson and Squyres (1990), at 100 K and 45 Hz is ~10^{-12} mho/cm, or 0.1 nS/m. This is a factor of ~10 too low (even if it made up the bulk of the subsurface and not just a thin upper layer) to account for the observed ~1 nS/m. However, Titan's surface is surely not pure polyacetylene –recent work on conductive polymers shows that other related compounds, notably polyaniline (which, like tholins, is a nitrogen-bearing material) can have very high conductivities- although we are unaware of cryogenic measurements.

8. Summary and conclusions

The present refined analysis of the PWA-MIP data provided a solid validation of the complex permittivity values at the Huygens landing site on Titan previously published in Grard et al., (2006) with the notable addition of reliable error bars. The values to remember for the 11 min after landing are 2.5±0.3 for the dielectric constant and 1.2±0.6 nS/m for the conductivity.

More surprising was the drop in the apparent permittivity of the environment detected at t=9539 s. It is now clear, at least at 45 Hz, that the apparent conductivity vanished below the measurement threshold at that time. A tentative scenario has been proposed wherein warming of volatile materials beneath the probe led to their sudden release, and the removal of some conductive material.

The fact that a significant feature of the surface dielectric properties (the conductivity) could be so rapidly removed suggests that it is not productive to try matching the apparent complex permittivity with a single underground component. On the contrary, it would be better to investigate more complex ground models, for instance those involving a thin superficial layer which configurations are supported by other instrumental data, as proposed in Atkinson et al., 2010. Following this approach the measured dielectric constant would be more representative of the bulk underground material, whereas the apparent conductivity should not be interpreted without any knowledge of the superficial layer, mainly its thickness. Laboratory

measurements of the conductivity of tholins (and other relevant materials such as polyaniline) that are supposed to fall on the surface of Titan would also help understanding the compositional properties observed at the Huygens landing site.

In conclusion the PWA-HASI experiment was the first, and successful, robotic attempt to measure in situ the complex permittivity of a planetary surface. Even before the landing of Huygens on Titan and the reception of the first data from another instrument, the Permittivity Probe (PP-SESAME, Seidensticker et al., 2007) on Philae, the lander of the ROSETTA mission, was prepared for investigating the Churyumov-Gerasimenko comet nucleus. The main improvements of this experiment with respect to PWA-MIP are the measurement of the emitted current and the use of an additional transmitter: both give access to inhomogeneities, close to the electrodes and at shallow depth, respectively. The few first PP-SESAME data collected in November 2014 on the nucleus are currently under analysis (Lethuillier et al., AGU 2014), and at the time of writing additional measurements are awaited as Philae has woken up from hibernation.

Acknowledgements

References

Alvarez, R., 1973. Permafrost: relation between ice content and dielectric losses at 100°K. Earth and planet. Sci. Lett. 20, 409-414.

Atkinson, K.R., and 10 colleagues, 2010. Penetrometry of granular and moist planetary surface materials: application to the Huygens landing site on Titan. Icarus, 210, 843-851, doi:10.1016/j.icarus.2010.07.019.

Béghin, C., Hamelin, M. and C. Sotin, 2010, Titan's native ocean revealed beneath some 45 km of ice by a Schumann-like resonance, Comptes Rendus Geoscience, 342, 425-433.

Béghin, C., and 4 colleagues, 2013, Observation of 2nd Schumann eigenmode on Titan's surface. Geosci. Instrum. Method. Data Syst., 2, 237-248, 2013.

Bettanini, C., M. Zaccariotto, F. Angrilli, 2008. Analysis of the HASI accelerometers data measured during the impact phase of the Huygens probe on the surface of Titan by means of a simulation with a finite-element model. Planet. Space Sci. 56, 715-727, doi:10.1016/j.pss.2007.10.010.

Cadène, F., 1995, Méthodologie de mesure de conductivité d'atmosphères planétaires, Ph.D. Thesis, UPMC, Paris, France (*in french*).

Clark, R.N., and 15 colleagues, Detection and mapping of hydrocarbon deposits on Titan, J. Geophysical Res. Planets, 115, E10005, doi:10.1029/2009JE003369.

Durand, E., 1966, Electrostatique, Problèmes généraux conducteurs, vol.2, Masson, Paris, pp. 154-155 (*in french*).

Eisenberg, D. and W. Kauzmann, 2005 The structure and properties of water, Oxford, doi: 10.1093/acprof:oso/9780198570264.001.0001.

Falkner, P., 2004, Permittivitäts Wellen und Altimeter Analysator für der ESA/NASA Projekt Cassini-Huygens. Ph.D. Thesis, Technical University, Graz, Austria (*in german*).

Fulchignoni, M., and 27 colleagues, 2002, The characterisation of Titan's atmospheric physical properties by the Huygens Atmospheric Structure Instrument (HASI), Space Sci. Rev. 104, 395-431.

Fulchignoni, M., and 42 colleagues, 2005, In situ measurements of the physical characteristics of Titan's environment. Nature 438 (8), 785-791, doi:10.1038/nature04314.

Grard, R., 1990a, A quadrupole system for measuring in situ the complex permittivity of materials: application to penetrators and landers for planetary exploration. Meas. Sci. Technol. 1, 801-806.

Grard, R., 1990b, A quadrupolar array for measuring the complex permittivity of the ground: application to Earth prospection and planetary exploration. Meas. Sci. Technol. 1, 295.

Grard, R., and 4 colleagues, 1995. An experimental investigation of atmospheric electricity and lightning activity to be performed during the descent of the Huygens Probe on Titan. J.Atm.Terr. Phys. 57, 575-585.

Grard, R., and 19 colleagues, 2006. Electric properties and related physical characteristics of the atmosphere and surface of Titan. Planet. Space Sci. 54, 1124-1136.

Griffits, C.A. and 4 colleagues. 2003, Evidence for the Exposure of Water Ice on Titan's Surface, Science, 300 (5619), 628-630.

Hamelin, M., and 17 colleagues, 2000, Surface and sub-surface electrical measurement of Titan with the PWA-HASI experiment on Huygens. Adv. Space Res., 26 (10), 1697-1704.

Hamelin, M., and 17 colleagues, 2007, Electron conductivity and density profiles derived from the mutual impedance probe measurements performed during the descent of Huygens through the atmosphere of Titan. Planet. Space Sci. 55, 1964-1977, doi:10.1016/j.pss.2007.04.008.

Jaumann, R., and 18 colleagues, 2008. Fluvial erosion and post-erosional processes on Titan. Icarus 197, 526-538, doi:10.1016/j.icarus.2008.06.002.

Jernej, I. and P. Falkner, 2004, HASI-PWA calibration document. HASI-PWA-FM-DOC-41, IWF, Austrian Academy of Sciences, Graz.

Karkoschka, E., and 6 colleagues, 2007. DISR imaging and the geometry of the descent of the Huygens probe within Titan's atmosphere. Planet. Space Sci. 55, 1896-1935, doi:10.1016/j.pss.2007.04.019.

Karkoschka, E., and M.G. Tomasko, 2009, Rain and dewdrops on Titan based on in situ imaging, Icarus 199, 442-448, doi:10.1016/j.icarus.2008.09.020.

Kawada, S., 1978, Dielectric anisotropy of ice Ih. J. Phys. Soc. Japan 44, 1881-1886.

Lebleu, D., Jun. 2005. Huygens Probe: Probe reference data for post fight analysis. Tech. Rep. HUY.ASP.MIS.TN.0006, Alcatel Space, Cannes, France.

Lebreton, J.-P., and D.L. Matson, 2002. The Huygens probe: science, payload and mission overview. Space Sci. Rev. 104, 59-100.

Lebreton, J.-P., and 12 colleagues, 2005. An overview of the descent and landing of the Huygens probe on Titan. Nature 438, 758-764, doi: 10.1038/nature04737.

Leese, M.R., and 3 colleagues, 2012. The Huygens surface science package (SSP): flight performance review and lessons learned. Planet. Space Sci.70, 28-45, doi:10.1016/j.pss.2012.06.005.

Le Gall et al., and 6 colleagues, 2012. Latitudinal and altitudinal controls of Titan's dune field morphometry. Icarus, 217, 231-242, doi:10.1016/j.icarus.2011.10.024.

Le Gall et al., 2015, Composition, seasonal change and bathymetry of Ligeia Mare, Titan, derived from its 2.2-cm thermal emission , submitted.

Lethuillier, A. and 6 colleagues, 2014, Measuring the permittivity of the surface of the Churyumov-Gerasimenko nucleus: the PP-SESAME experiment on board the Philae/ROSETTA lander, *AGU Fall Meeting 2014*, Dec 2014, San Francisco, United States. pp.P34B-05.

Lopes, R.M.C., and 24 colleagues, 2010. Distribution and interplay of geological processes on Titan from Cassini radar data. Icarus 205, 540-558, doi:10.1016/j.icarus.2009.08.010.

López-Moreno, J.J., and 16 colleagues, 2008. Structure of Titan's low altitude ionized layer from the relaxation probe onboard Huygens. Geophys. Res. Lett. 35, L22104, doi:10.1029/2008GL035338.

Lorenz, R., and 4 colleagues, 2006. Titan's damp ground : constraints on Titan surface properties from the temperature evolution of the GCMS inlet. Meteoritics & Planetary Science 41 (11), 1705-1714.

Lorenz, R.D., and 8 colleagues, 2014. Silence on Shangri-La: attenuation of Huygens acoustic signals suggests surface volatiles. Planet. Space Sci. 90, 72-80, doi.org/10.1016/j.pss.2013.11.003.

Lorenz, R., and 10 colleagues, 2015, Observations of the surface of Titan by the radar altimeters on the Huygens probe, submitted to Icarus.

Mattei et al., 2014, Dielectric measurements and radar attenuation estimation of ice/basalt sand mixtures as martian Polar Caps analogues, Icarus 229, 428–433.

Mitchell, K. L., and 4 colleagues, 2015, Laboratory measurements of cryogenic liquid alkane microwave absorptivity and implications for the composition of Ligeia Mare, Titan, Geophys. Res. Lett., 42.

Niemann, H.B., and 17 colleagues, 2005, The abundances of constituents of Titan's atmosphere from the GCMS instrument on the Huygens probe. Nature, 438 (8), 779-784, doi:10.1038/nature04122.

Niemann, H.B., and 9 colleagues, 2010, Composition of Titan's lower atmosphere and simple surface volatiles as measured by the Cassini-Huygens probe gas chromatograph mass spectrometer experiment. J. Geophys. Res. 115, E12006, doi:10.1029/2010JE003659.

Paillou, P., and 4 colleagues, 2008, Microwave dielectric constant of Titan-relevant materials. Geophys. Res. Lett. 35, L18202, doi:10.1029/2008GL035216.

Pérez-Ayúcar, M., and 4 colleagues, 2006, Surface properties of Titan from post-landing reflections of the Huygens radio signal. JGR Planets, 111, E07001, doi:10.1029/2005JE002613.

Petrenko, V.F. and R.W. Whitworth, 1999, Physics of ice, 373pp, Oxford University Press.

Radebaugh, J., and 20 colleagues, 2011, Regional geomorphology and history of Titan's Xanadu province. Icarus 211, 672-685, doi: 10.1016/j.icarus.2010.07.022.

Schröder, S.E., E. Karkoschka, R. Lorenz, 2012, Bouncing on Titan: motion of the Huygens probe in the seconds after landing. Planet. Space Sci. 73, 327-340, doi:10.1016/j.pss.2012.08.007.

Seidensticker, K.J., and 10 colleagues, 2007, SESAME - An Experiment of the Rosetta Lander Philae: Objectives and General Design, Space Sci. Reviews, 128, 301-337.

Simões, F., 2007, Theoretical and experimental studies of electromagnetic resonances in the ionospheric cavities of planets and satellites; instrument and mission perspectives, PhD thesis, University Pierre and Marie Curie, Paris.

Sotin, C., and 25 colleagues, 2005, Release of volatiles from a possible cryovolcano from near-infrared imaging of Titan. Nature 435 (9), 786-789, doi:10.1038/nature03596.

Storey, L.R.O., Aubry, M.P., Meyer, P., 1969, A quadrupole probe for the study of ionospheric resonances. In Thomas, J.O., Landmark, B.J. (Eds.), Plasma waves in space and in the laboratory, Edinburgh University Press, 303-332.

Thompson, W.R. and S.W. Squyres, 1990, Titan and other icy satellites: dielectric properties of constituent materials and implications for radar sounding. Icarus 86, 336-354.

Tobie, G., and 4 colleagues, 2005, Titan's internal structure inferred from a coupled thermal–orbital model, Icarus, 175, 496-502, doi:10.1016/j.icarus.2004.12.007.

Tomasko, M.G., and colleagues, 2005, Rain, winds and haze during the Huygens's descent to Titan's surface. Nature 438 (8), 765-778, doi:10.1038/nature04126.

Towner, M.C., and 8 collegues, 2006, Physical properties of Titan's surface at the Huygens landing site from the Surface Science Package Acoustic Properties sensor (API-S), Icarus 185, 2006; 457-465, doi:10.1016/j.icarus.2006.07.013.

Trautner, R., Falkner, P., 2000, Equivalent circuit model, systematic error calculation and measurement range estimation for HASI-PWA mutual impedance (MI) probe. Internal report, ESA/ESTEC, April 12, 2000.

Wenner, F., 1915, A method of measuring the Earth resistivity. U.S. Bur. Stand. Bull. Sci. Pap. 25 (12), 469-478.

Williams, K.E., C.P. McKay, F. Persson, 2012, The surface energy balance at the Huygens landing site and the moist surface conditions on Titan. Planet. Space Sci. 60, 376-385, doi:10.1016/j.pss.2011.11.005.

Zarnecki, J.C., and 4 colleagues, 2002, Huygens's surface science package. Space Sci. Rev. 104, 593-611.

Zarnecki, J.C., and 25 colleagues, 2005, A soft solid surface on Titan as revealed by the Huygens Surface Science Package. Nature 438 (8), 792-795, doi:10.1038/nature04211.

Annex I

Capacity-Influence matrix of a system of electrodes in the case of two homogeneous media separated by a plane interface (but not touching the interface)

The problem was studied in the case of pin-point electrodes in Grard (1990a and 1990b) . We intend to generalize the results to the case of real size electrodes. Without attempt to the general case we will assume a vacuum and a normalized permittivity 1 for the upper half space A and ε^* for the lower half space B. All conductors are in domain A. For conductor k, the superficial density of charge being $q_s(\mathbf{r})$ at a point $\mathbf{r}$ of the surface, the charge of a small surface element dS can be represented by a point charge $dq = q_s(\mathbf{r})$ dS at point $\mathbf{r}$. The contribution of potential dV due to charge dq at some point $\mathbf{r_p}$ of the upper half space A is:

$$dV = (dq / 4 \pi \varepsilon_0) [1/r_0 + ((1-\varepsilon^*) / (1+\varepsilon^*)) / r_1] \qquad (I1.1)$$

r_0 : distance $|\mathbf{r}-\mathbf{r_p}|$

r_1 : distance $|\mathbf{r_s}-\mathbf{r_p}|$, where $\mathbf{r_s}$ is the symmetrical point of $\mathbf{r}$ with respect to the interface.

Let us consider now two basic configurations C_0 and C_M.

For C_0, the full set of conductors is in infinite vacuum; for the same charge element than before the potential contribution at $\mathbf{r_p}$ (the interface is virtual) is:

$$dV_0 = (dq / 4 \pi \varepsilon_0) [1/r_0] \qquad (I1.2)$$

For C_M, in a upper half vacuum space limited by a perfectly conductive plane interface, the resulting potential is the sum of potentials induced by the charge and its mirror charge :

$$dV_M = (dq / 4 \pi \varepsilon_0) [1/r_0 - 1/r_1] \qquad (I1.3)$$

From these equations we found that the configuration with the electrode system above a half space of conductivity ε can be described as the weighted sum of the two basic configurations C_0 and C_M:

$$dV = (2 / (1+\varepsilon^*)) dV_0 + ((\varepsilon^*-1) / (1+\varepsilon^*)) dV_M \qquad (I1.4)$$

Then only two configurations C_0 and C_M need to be analysed (numerically or with calibrations) to provide the two capacity-influence matrices **[C$_0$]** and **[C$_M$]**. The vectors of potentials for all electrodes are :

$\mathbf{V_0} = [\mathbf{C_0}]^{-1} \, \mathbf{Q}$ and $\mathbf{V_M} = [\mathbf{C_M}]^{-1} \, \mathbf{Q}$ (I1.5)

After the weighted superposition we get:

$\mathbf{V} = \mathbf{V_0} + \mathbf{V_M} = \{ (2 / (1+\varepsilon^*)) \, [\mathbf{C_0}]^{-1} + ((\varepsilon^*-1) / (1+\varepsilon^*)) \, [\mathbf{C_M}]^{-1} \} \, \mathbf{Q}$ (I1.6)

and the full configuration can be represented by the composite matrix:

$[\mathbf{C}] = \{ (2 / (1+\varepsilon^*)) \, [\mathbf{C_0}]^{-1} + ((\varepsilon^*-1) / (1+\varepsilon^*)) \, [\mathbf{C_M}]^{-1} \}^{-1}$ (I1.7)

When the electrodes are in both sides of the interface the same procedure can be used with three basic configurations with:

C_0 (infinite vacuum), with all conductors, giving matrix $[\mathbf{C_0}]$

C_A with only conductors of A and their images in B, giving matrix $[C_A]$

C_B with only conductors of B and their images in A, giving matrix $[C_B]$

For configuration C_0, as before we have (with all conductors):

$\mathbf{V_0} = [\mathbf{C_0}]^{-1} \, \mathbf{Q}$ (I1.8)

For the two 'mirror' configurations C_A and C_B we will define $[\mathbf{C_{AB}}]$ **by**

$\mathbf{V_{AB}} = [\mathbf{C_{AB}}]^{-1} \, \mathbf{Q}$ (I1.9)

With combination of sub-matrices:

$$[\mathbf{C_{AB}}]^{-1} = \begin{array}{|c|c|} \hline ((\varepsilon^*-1)) / (\varepsilon^* +1)) \; [C_A]^{-1} & [0] \\ \hline [0] & (1/\varepsilon^*)((\varepsilon^*-1)) / (\varepsilon^* +1)) \; [C_B]^{-1} \\ \hline \end{array}$$

(II.10)

These formulas allow easy computation of potential vectors for any value of the complex permittivity in the case of a plane interface, separating the geometry factor from the permittivity factor, but they cannot be used when any electrode crosses the interface. Then the representative matrices are calculated for both geometry and complex permittivity values.

Annex II

PWA-MIP preamplifiers and receiving circuit calibration adjustments.

General preamplifiers setup

The best location for receiving preamplifiers is directly attached to electrodes but, for avoiding the problems of low and uncontrolled temperature environment they were installed in the small HASI-I boxes inside the heated Huygens capsule. The ring electrodes were linked to the preamplifiers via small coupling capacitors and through triaxial cables, without any connector (HASI-I boxes were small enough to be introduced through dedicated windows into the capsule equatorial ring). The electronic circuit model is shown in fig. II.1. The signal is fed into a low input impedance operational amplifier (OA) AD549 that drives the active shield of the cable to about the same voltage than the input, annihilating the apparent cable capacitance and allowing to drive a ~1.4 m long cable. Moreover, protection diodes were installed to avoid propagation of possible atmospheric discharges inside the capsule, but in principle they do not affect the MIP small signals. The problem of this setup is that the values of the very small coupling and input capacitors are known with poor accuracy before assembly. Laboratory calibrations and modelling allow deriving the hidden characteristics of the circuit.

Laboratory calibrations; temperature effect.

The calibrations of the flight model (FM) have been performed in two ways:

- Calibration of PWA-MI receiving part (PWA-AC for passive measurements, preamplifiers + filters) from electrode to ADC point, at room temperature in the laboratory (Jernej and Falkner, 2004).

- Special calibrations of the preamplifiers connected to the electrodes: preamplifiers at room temperature, but with two conditions for the booms: either at room temperature or at LN2 (liquid nitrogen) temperature in a cooling chamber. This last setup corresponds roughly to the case of the descent in the atmosphere of Titan.

The difference between the two 'warm' and 'cold' cases is only due to the coupling capacitor circuits located inside the booms close to the RX electrodes. It determines the correction to apply to 'warm' calibrations when the booms are at Titan temperature.
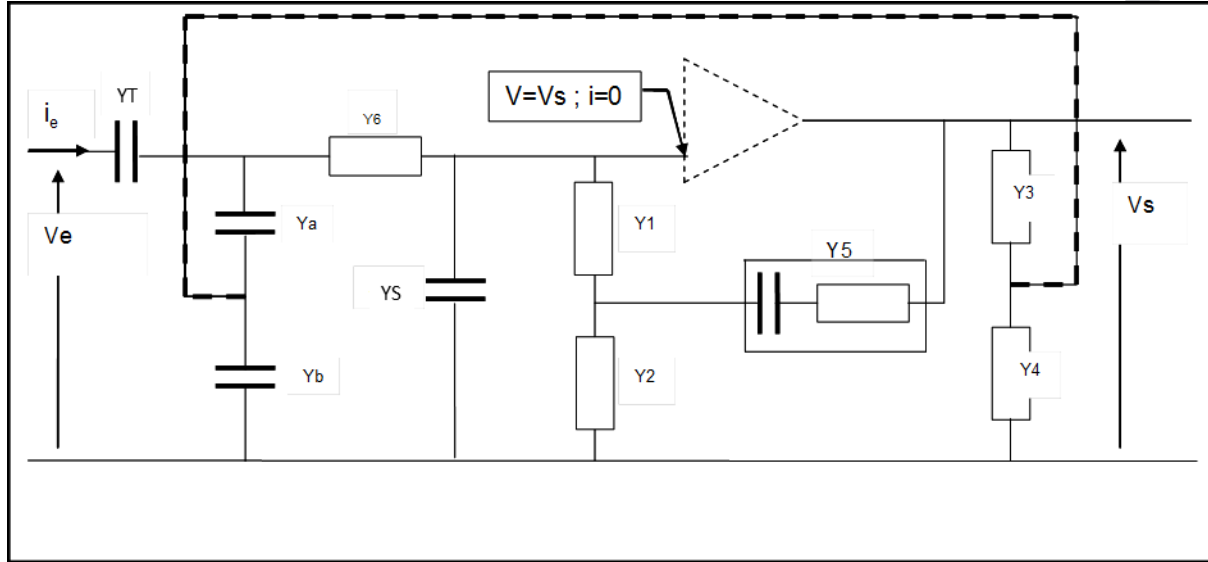

Figure II.1. MI preamplifier model. Y_T is the C_T coupling capacitor admittance (close to the Rx electrode). Y_S is the C_S stray capacitor admittance. Ya and Yb are the admittances of the triaxial cable (respectively inner to intermediate and intermediate to outer shields). Component nominal values: Y_1 and Y_2: 10 MΩ; Y_3: 51 Ω ; Y_4: 51 kΩ ; Y_5 : 3.01 Ω − 5.2 µF ; Y_a and Y_b : triaxial cable capacitances of 88 and 289 pF/m respectively.

Analytical formulas and curve fitting

The circuit equations lead to analytical formulas for the gain and input impedance of the circuit, depending on the nominal component values, except for Y_T and Y_S of figure II.1, and also Ya and Yb that represent the inner and outer capacitances of the triaxial cable. Then these hidden parameters are determined using a least-square procedure applied to the laboratory calibration data. The transfer function amplitudes are shown in Fig. II.2 for the 'warm' and 'cold' situations and for the difference.

The formula of the gain in the 'cold' situation as on Titan is shown in Table 2 of the paper as a rational function with the 8 numerical corresponding coefficients.

Coupling capacitance and input capacitance values

In practice, both C_T (less than 0.5 pF) and Y_S (OA input capacitance, 0.8 pF from data sheet) are difficult to measure separately. Last and not the least the circuits are covered with a protective deposit that changes these capacitances. The best fit between calibration data (preamplifier at room temperature but electrodes and coupling circuit at ~-180° C), with the model was found for the values $C_T = 0.3678$ pF, $C_S = 1.255$ pF, and for cable lengths of 1.409 m.
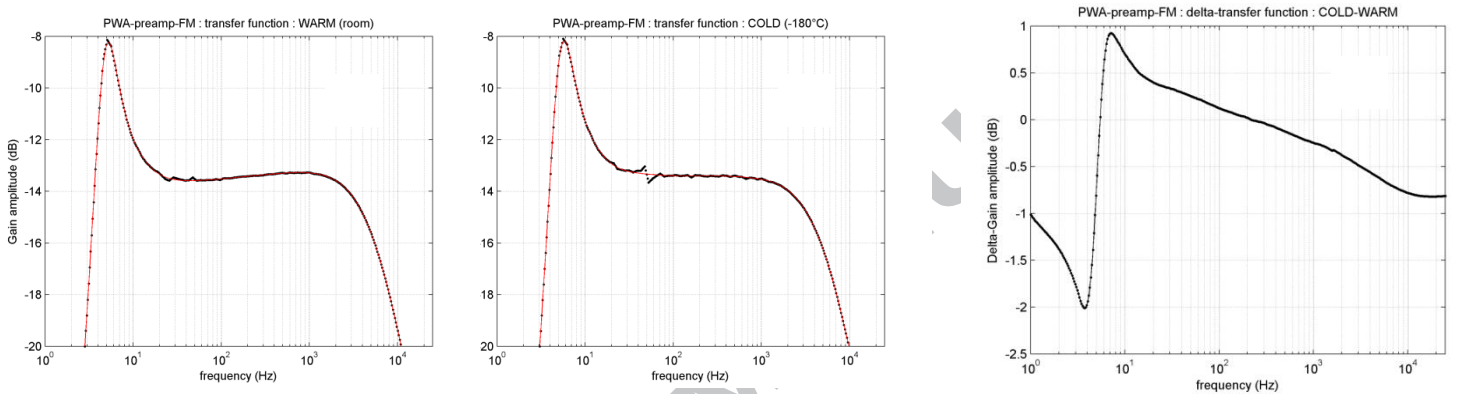

Figure II.2. a and b: MIP preamplifier amplitude of transfer function for 'warm' and resp. 'cold' conditions. Black: experimental calibration values; red: analytical function. c: differential value for correction of the full receiver calibration performed at room temperature.

The analytical transfer functions matches very accurately the calibration data (except at ~50 Hz, frequency of electrical power distribution in the laboratory), supporting the value adopted for C_T and C_S.

The electrical properties of Titan's surface at the Huygens landing site measured with the PWA-HASI Mutual Impedance Probe. New approach and new findings

Michel Hamelin[1,2], Anthony Lethuillier [1,2], Alice Le Gall[1,2], Réjean Grard[3], Christian Béghin[4], Konrad Schwingenschuh[5], Irmgard Jernej[5], José-Juan López-Moreno[6], Vic Brown[6], Ralph D. Lorenz[7], Francesca Ferri[8], Valérie Ciarletti[1,2]

Highlights:

- We assess the dielectric constant and electrical conductivity of Titan's ground at the Huygens landing site
- We analyze a fast change of electrical characteristics of the ground observed 11 min after Huygens landing
- A scenario involving a gas outburst triggered by Huygens heat is proposed